DR. FABRIZIO TURSI (Orcid ID : 0000-0001-7269-2753)

Article type : Original Article

What can high-pressure sheared orthogneisses tell us? An example from the Curinga–Girifalco Line (Calabria, southern Italy)

Fabrizio Tursi[1], Pasquale Acquafredda[1], Vincenzo Festa[1], Annamaria Fornelli[1,*], Antonio Langone[2], Francesca Micheletti[1], Richard Spiess[3]

[1]Dipartimento di Scienze della Terra e Geoambientali, Università degli Studi di Bari "Aldo Moro", Bari, Italy.

[2]Dipartimento di Scienze della Terra e dell'Ambiente, Università degli Studi di Pavia, Pavia, Italy.

[3]Dipartimento di Geoscienze, Università degli Studi di Padova, Padova, Italy.

[*]Corresponding author: annamaria.fornelli@uniba.it

Abstract

High-pressure (*HP*) mineral parageneses are usually poorly developed within metagranitoids, as these rocks are commonly affected by fluid-deficient conditions when experiencing a

metamorphic cycle. However, since ductile shear zones can act as preferential pathways for fluids in the Earth's crust, if metagranitoids are involved in ductile shear under *HP* conditions, the presence of fluids during deformation can induce recrystallisation and equilibration in these rocks. With this in mind, we investigate the formation and evolution of mineral assemblages in the orthogneisses of the Castagna Unit from the northern Serre Massif (Calabria, southern Italy). During Alpine tectonics, the thrusting along the Curinga–Girifalco Line juxtaposed these rocks, representative of the Hercynian intermediate crust, below the lithologies of the Hercynian lower crust. A detailed microstructural study of the orthogneisses, sampled along a progressively increasing ductile deformation gradient, revealed a variation in the mineral assemblage between the weakly-deformed orthogneisses and those in the shear zone. Phase diagram calculations in the MnNCKFMASHTO system indicate that the progressive replacement of relict minerals by new, Alpine minerals in the shear zone, was related to the presence of fluids during deformation. This allowed equilibration of the sheared orthogneisses up to metamorphic peak conditions of ~0.9–1.0 GPa and ~560–590 °C. Our integrated study highlights that both weakly-deformed and mylonitic orthogneiss share the same peak metamorphic conditions, and that the new equilibrium mineral assemblage was stabilised in the mylonitic orthogneisses along a fluid-conservative prograde path, where no fluid was added or lost. After metamorphic peak, the fluid was channelled towards the inner part of the shear zone, with fluid-present conditions that were restricted to the mylonitic orthogneisses close to the tectonic contact. These mylonitic orthogneisses record cooling and exhumation to 0.6–0.7 GPa and 360–400 °C, showing an overall anticlockwise *P*–*T* path. By comparing our findings with existing structural studies, we highlight that the Castagna Unit was under-thrusted to lower-crustal depths during the Alpine orogeny, before the re-activation of the Curinga–Girifalco Line during the Oligocene to Miocene extensional tectonic phase, that enabled the exhumation of this unit.

Keywords: HP-metagranitoids, ductile shear zones, anticlockwise *P*–*T* path, Alpine Calabria, fluid–rock interactions

1 INTRODUCTION

Modelling the pressure (*P*)–temperature (*T*) path of metagranitoids that experienced *HP*-metamorphism is one of the most intriguing challenges in metamorphic petrology. This is because, under closed-system conditions, the (very) low fluid content in these rocks, which is inherited from the magmatic protolith, commonly hinders the development of *HP*-parageneses (e.g. Biino & Compagnoni, 1992; Compagnoni & Rolfo, 2003; Massonne, 2015; Proyer, 2003). The most recurrent *HP*-index mineral in metagranitoids is garnet, which is characterised by a $X_{Ca} > 0.2$ (Carswell, Wilson, & Zhai, 2000; Le Goff & Ballèvre, 1990; Massonne, 2015; Proyer, 2003) and is commonly associated with quartz + K-feldspar + albite + phengite + epidote + sphene/rutile ± biotite (Carswell et al., 2000; Giuntoli, Lanari, Burn, Kunz, & Engi, 2018; Le Goff & Ballèvre, 1990; Maldonado, Ortega-Gutiérrez, & Ortíz-Joya, 2018; Massonne, 2015; Menold et al., 2009; Proyer, 2003; Xia, Zheng, Lu, Hu, & Xu, 2012; Young & Kylander-Clark, 2015; Zucali, 2011).

Le Goff & Ballèvre (1990) demonstrated the problematic uses of conventional thermobarometers to estimate *P*–*T* conditions for the metamorphic peak in *HP*-metagranitoids. According to these authors, (i) the garnet–biotite Fe–Mg thermometer suffers from problems related to the high-grossular activity of garnet when it is applied to these rocks, and (ii) the phengite barometer of Massonne & Schreyer (1987) needs independent temperature estimate along with corrections for the Fe–Mg partitioning between phengite and biotite.

Another crucial aspect of *HP*-metagranitoids concerns the usual presence of corona textures and non-concentric zoning patterns of garnet and white mica (e.g. Bruno et al., 2001; Zucali, 2011), which reflect local equilibration. In addition to the local equilibration affecting these rocks, the Fe-rich composition of garnet, at a *P* of ≥ 1.0 GPa, suggests H_2O-undersaturated conditions (Proyer, 2003).

According to Pattison, de Capitani, & Gaidies (2011) and Pattison & Tinkham (2009), the catalytic role exerted by fluids on metamorphic reactions could be critical for the (i) stabilisation of *HP*-mineral assemblages in metagranitoids, and (ii) their preservation or restoration during exhumation (Guiraud, Powell, & Rebay, 2001; Proyer, 2003; Young & Kylander-Clark, 2015). Proyer (2003) investigated the preservation of HP mineral assemblages

in metagranitoids in relation to the rock's fluid budget. The author concluded that: "… *Metagranitoids do not easily record or preserve high pressure conditions, either because of metastable persistence throughout the high-pressure section of the P–T path or because of significant dehydration during exhumation* …". More recently, Young & Kylander-Clark (2015) conducted a comparative thermodynamic study among different lithologies that were metamorphosed at *HP*-conditions, considering also metagranitoids. The authors investigated whether the mineral assemblage of these rocks was prograde or retrograde with respect to the peak metamorphic conditions attained, considering the available fluid-budget in the rock with respect to the modes of the OH-bearing minerals. In contrast to Proyer (2003), Young & Kylander-Clark (2015) concluded that *HP*-metagranitoids should retain part of their prograde mineral assemblages but should not convert further without additional water influx. Moreover, the breakdown of OH-bearing minerals, such as white-mica, during exhumation may not trigger a complete retrogression in HP-metagranitoids, as a result of the low modal abundance of these mineral phases in these rocks. Furthermore, it is well known that deformation can also play a major role in promoting mineral stabilisation (Bell & Hayward, 1991; Holyoke & Tullis, 2006; Waters & Lovegrove, 2002). In this sense, ductile shear zones that developed in felsic rocks are an ideal setting to study deformation-enhanced recrystallisation, particularly if deformation was coupled to fluid–rock interactions during shearing (e.g. Tursi, Festa, Fornelli, Micheletti, & Spiess, 2018, and references therein).

Therefore, to investigate the role of fluid in the stabilisation of mineral *HP*-parageneses in deformed metagranitoids, a case where these rocks were affected by ductile shearing is considered in the present study. In particular, the orthogneisses of the Castagna Unit that outcrop along the Curinga–Girifalco Line (CGL) in the northern Serre Massif (Calabria, southern Italy) are focussed on. The reconstruction of the *P–T–fluid* path that was experienced by these rocks is attempted for the first time, relating the mineral compositions and zoning patterns of phengite and garnet to the fluid-present/deficient conditions during shearing.

2 GEOLOGICAL SETTING

The Calabria–Peloritani terrane (Figure 1a) (Amodio-Morelli et al., 1976; Bonardi, Cavazza, Perrone, & Rossi, 2001) is an orogenic pile consisting of three main groups of stacked tectonic units (Figure 1b). From the bottom to the top, these can be summarised as follows: (i) the Lower Complex, which is characterised by Apennine units with Meso-Cenozoic phyllites and partly metamorphosed carbonate rocks showing a *HP* (~1.4 GPa) and low-*T* (*LT*) (~390 °C) metamorphic imprint (Iannace et al., 2007); (ii) the Intermediate Complex, which is composed of ophiolite units of the Ligurian Tethys' oceanic lithosphere (Liberi, Morten, & Piluso, 2006), that records *HP/LT* Eocene metamorphism with peak conditions at ~2.0–2.1 GPa and 470–490 °C (Tursi, Bianco, et al., 2020); (iii) the Upper Complex, which consists of an Hercynian continental crust (Ogniben, 1969), showing a local Alpine metamorphic overprint at 0.3–0.7 GPa and 200–450 °C in the Sila Massif and Catena Costiera (Acquafredda, Lorenzoni, & Zanettin Lorenzoni, 1994; Graessner & Schenk, 2001; Liberi, Piluso, & Langone, 2011; Ortolano et al., 2020; Piccarreta, 1981) and up to 1.1–1.2 GPa and 540–570 °C in the Aspromonte Massif (Cirrincione, Ortolano, Pezzino, & Punturo, 2008).

In Calabria, the Upper Complex is composed from the bottom to the top, of: (i) the Fiume Pomo Unit (Colonna, 1998), (ii) the Castagna Unit (Paglionico & Piccarreta, 1976), and (iii) the Sila and Serre Unit (Figure 1b) (Festa, Messina, Paglionico, Piccarreta, & Rottura, 2004, and references therein). In this study we focus on the tectonic contact between the Castagna and the Sila and Serre units.

The Castagna Unit primarily consists of late-Hercynian, low-amphibolite-facies orthogneisses, minor paragneisses and amphibole-bearing lenses (e.g. Colonna & Piccarreta, 1975). The orthogneisses have magmatic protoliths dated at *c.* 545 Ma (Fornelli, Festa, Micheletti, Spiess, & Tursi, 2020; Micheletti, Barbey, Fornelli, Piccarreta, & Deloule, 2007; Micheletti, Fornelli, Piccarreta, & Tiepolo, 2011) and show bulk chemical compositions ranging from granite to granodiorite (Fornelli, Micheletti, & Piccarreta, 2007). The primary magmatic and sedimentary rocks of the Castagna Unit were involved in the Hercynian orogeny under lower amphibolite-facies conditions (Brandt & Schenk, 2020; Ortolano et al., 2020), and subsequently in the Alpine tectonics.

The Sila and Serre Unit consists of a nearly complete Hercynian continental crust section with a thickness of ~22–23 km (e.g. Caggianelli, Prosser, Festa, Langone, & Spiess, 2013). From the bottom to the top, the Sila and Serre Unit comprises: (i) lower crustal mafic and felsic granulites that are overlain by migmatitic paragneisses (Schenk, 1980); (ii) tonalitic to granitic igneous bodies emplaced at mid-crust levels at around 280–300 Ma (Caggianelli, Prosser, & Rottura, 2000; Caggianelli et al., 2013; Langone, Caggianelli, Festa, & Prosser, 2014); (iii) upper crust amphibolite to greenschist facies paragneisses and phyllites (Angì et al., 2010; Festa, Caggianelli, Langone, & Prosser, 2013; Festa, Tursi, Caggianelli, & Spiess, 2018; Tursi, Spiess, Festa, & Fregola, 2020).

In the northern Serre Massif, the Castagna Unit and the lower crust rocks of the Sila and Serre Unit are juxtaposed along a prominent Alpine tectonic contact: the CGL (Langone et al., 2006; Schenk, 1980, 1981; Spiegel, 2003), which is characteristically exposed in the Girifalco locality (Figure 1c). According to Schenk (1981) and Langone et al. (2006), the Castagna Unit is overlain by the Sila and Serre Unit along this shear zone (Figure 2). Here, ductile deformation dated at *c.* 43 Ma by Schenk (1980) through the Rb-Sr isotopic system on biotite, has developed a considerable thickness of mylonitic rocks (~200–400 m) in both units (Langone et al., 2006; Paglionico & Piccarreta, 1976, 1978; Spiegel, 2003). According to Langone et al. (2006), the Alpine metamorphic overprint is recorded in the orthogneisses of the Castagna Unit by garnets showing grossular-poor core with grossular-rich overgrowths, and by the occurrence of new, fine-grained phengitic white mica. These authors applied conventional geothermobarometers to orthogneisses and amphibolite lenses, and estimated the *P*–*T* conditions of ductile shearing to be approximately 0.75–0.9 GPa and 525–570 °C. Similar *P*–*T* estimates were obtained for the sheared pseudotachylyte veins and the ultramylonitic layers that affect the mylonitic lower crustal rocks of the Sila and Serre Unit near the tectonic contact with the Castagna Unit orthogneisses (Altenberger, Prosser, Grande, Günter, & Langone, 2013; Altenberger, Prosser, Ruggiero, & Günter, 2011). Later, (late Eocene?)early Oligocene–early Miocene (30–15 Ma) extensional shearing and re-activation occurred along the CGL (Festa, Cicala, & Tursi, 2020), with cataclasites and un-sheared pseudotachylyte veins that developed at $T < 300$ °C (Thomson, 1998) in a brittle environment, in confinement to the tectonic contact (Langone et al., 2006;

Spiegel, 2003).

2.1 Orthogneiss field-geology and sampling

The shearing effects produced by Alpine ductile deformation on the orthogneiss of the Castagna Unit are evident alongside transects from the host-rock towards the contact with the Sila and Serre Unit, especially in the Pesipe Stream valley (Figure 2). Here, Festa et al. (2020) interpreted the mylonitic foliation S_m, in terms of map scale S-planes and C-type shear bands, and calculated a remarkable thickness of ~700 m for the mylonitic orthogneiss of the CGL (Figure 2).

The weakly deformed orthogneiss (Figure 3a) contains centimetre in size K-feldspar and quartz porphyroclasts (or "augen") (e.g. Figure 3b) in a grey–white quartz–feldspathic fine-grained matrix, that alternates with mica-rich layers, dominated by biotite. Moving towards the contact with the Sila and Serre Unit, a progressive grain size reduction of the K-feldspar and quartz porphyroclasts (up to millimetre in size), characterises the mylonitic orthogneisses (Figure 3c–f). The variations in the mineral assemblage, that are associated with the grain size reduction along the transect in Figure 2, are highlighted in the following by referring to samples collected approaching the contact with the Sila and Serre Unit, namely from weakly-deformed orthogneiss (sample VF80GR) to mylonitic orthogneiss (sample VF77GR) and mylonitic leucocratic orthogneiss (sample VF79GR).

3 MICROSTRUCTURES AND MINERAL CHEMISTRY

3.1 Methods

Samples have been characterised using a scanning electron microscope (SEM) of LEO, model EVO-50XVP, housed at the Department of Earth and Geo-environmental Sciences, University of Bari Aldo Moro, coupled with an X-max (80 mm^2) energy-dispersive (ED) Silicon drift Oxford detector (Oxford Instruments, High Wycombe, Buckinghamshire, UK) equipped with a Super Atmosphere Thin Window ©. Microanalysis was performed with the Silicon drift energy-dispersive detector on polished thin sections. Quantitative results were obtained using operating conditions of 15 kV accelerating potential, 500 pA probe current, about 25,000 output counts per second (cps) as average count rate on the whole spectrum, counting time of 50 s and

8.5 mm working distance. X-ray intensities were converted to wt.% (w/w) oxides by XPP correction scheme developed by Pouchou & Pichoir (1988, 1991), granted as quantitative software support by Oxford-Link Analytical (U.K.). Given the composition of the analysed mineral phases, the 1σ precision corresponded to the following values: SiO_2 = 0.10–0.20 wt.%, TiO_2 = 0.08–0.10 wt.%, Al_2O_3 = 0.08–0.13 wt.%, FeO = 0.05–0.15 wt.%, MnO = 0.04–0.6 wt.%, MgO = 0.08–0.13 wt.%, CaO = 0.04–0.14 wt.%, Na_2O = 0.04–0.06 wt.% and K_2O = 0.04–0.12 wt.%. The accuracy of the analytical data was also checked using several standard minerals manufactured by Micro-Analysis Consultants Ltd. (U.K.); four of the standards used for element calibrations (augite, almandine, pyrope and orthoclase) are reported as supplementary data in Table S1. All the analyses of the relevant minerals (i.e. garnet, micas and feldspars) used to constrain the thermobarometric evolution of the Castagna Unit's orthogneisses in this study are provided in the supplementary Table S2. The bulk rock compositions (Table 1) were obtained by X-ray fluorescence analysis using a Panalytical AXIOS-Advanced spectrometer equipped with a 4 kW Rh Super Sharp end window X-ray Tube at the Department of Earth and Geo-environmental Sciences, University of Bari Aldo Moro. XRF-analysis was conducted on pressed powders of thin section back cut after a careful microstructural survey, in order to exclude any possible polymetamorphic chemical zoning of key mineral phases like garnet (e.g. Argles, Prince, Foster, & Vance, 1999; Palin, Weller, Waters, & Dyck, 2016). The operating conditions of the XRF spectrometer were: 60 kV and 66 mA the X-ray tube power supply; a scintillator detector was used to collect the X-ray lines dispersed by a LiF 220 crystal. X-ray intensities were converted in oxide wt.% using the mathematical matrix correction procedure as suggested by (Leoni & Saitta, 1976a, 1976b) and (Leoni, Menichini, & Saitta, 2004). Two reference standards (AGV-1 from USGS-USA and NIM-G from NIM-South Africa) were used to check the accuracy of the analytical data: the precision is better than 3% for all elements. The water content of the rock was measured as loss on ignition (LOI), heating the powdered samples at 900°C for 12 hours. This value takes into account the loss of OH from hydrous silicates, the CO_2 from carbonate dissociation and of S, Cl and other anions due to the dissociation of sulphides, sulphates, chlorides.

3.2 Weakly-deformed orthogneiss

Sample VF80GR is a weakly-deformed orthogneiss (Figures 3a, b) with large K-feldspar, plagioclase and quartz porphyroclasts (up to 2 cm in size) that are dispersed into a matrix with anastomosing quartzofeldspathic and mica-rich layers (Figure 4a, b). The mineral assemblage comprises quartz + K-feldspar + plagioclase + biotite + muscovite + epidote + sphene + ilmenite + apatite. The plagioclase in the matrix is fine-grained recrystallised and shows an albite composition with an X_{An} of ~0.06, whereas the plagioclase porphyroclasts are oligoclase in composition with an X_{An} of ~0.12 (Table 2). Biotite occurs in flakes up to ~300 μm in size aligned to the main foliation (Figure 4b), and is characterised by ~1.55 apfu (atoms per formula unit) of Al, ~0.11 apfu of Ti, and an X_{Fe} ratio (as $Fe^{2+}/(Fe^{2+} + Mg)$) of ~0.6 (Table 2). In most of cases, biotite is observed to be wrapped by tiny (up to ~50 μm in size) white mica-rich layers (Figure 4b) that displayed Si = 3.28–3.36 apfu and X_{Fe} = 0.38–0.44 (Table 2). The Si content of this tiny white mica is higher than the Si = 3.11–3.15 apfu measured on the larger muscovite flakes (up to ~250 μm in size), the latter also characterised by X_{Fe} = 0.48–0.51 (Table S2). The epidote grains have a subhedral shape (Figures 4a, c) and are found either replacing large plagioclase porphyroclasts (Figure 4a) or within the matrix aligned to the main foliation (Figure 4c). Epidote grains are characterised by ~2.42 apfu of Al and ~0.51 apfu of Fe^{3+} (Table 3). Ilmenite is the prevalent opaque mineral in the rock, characterised by ~0.10 apfu of Mn (Table 3). Ilmenite also commonly has overgrowths of small titanite coronae (Figure 4c), with Al and Fe^{3+} of ~0.08 apfu and ~0.01 apfu, respectively (Table 3).

3.3 Mylonitic orthogneisses

3.3.1 Sample VF77GR

Sample VF77GR is a garnet-bearing mylonitic orthogneiss (Figures 3c, d), which is characterised by K-feldspar, quartz, and minor plagioclase porphyroclasts, set in a fine-grained matrix with anastomosing quartzofeldspathic layers alternating with very thin white-mica layers (Figures 4d, e). Quartz + K-feldspar + plagioclase + white mica + garnet + epidote + sphene ± biotite ± ilmenite constitute the mineral assemblage of this sample (Figures 4d–f). K-feldspar and plagioclase within the matrix are fine-grained and recrystallised (Figure 4d), with the

plagioclase being close to the pure albite in composition (X_{An} = 0.01) (Table 2). Garnet grains, up to ~200 μm in size, are present in the rock (Figure 4e, f); they have an ellipsoidal shape and are wrapped by the main mylonitic foliation (Figure 4e, f). Garnets commonly host tiny inclusions of quartz, albite, white mica and sphene (Figures 4f and 5a, b); epidote and chlorite are sometimes observed around the crystals (Figure 5a, b). Garnets have grossular-rich compositions (Table 4) and show appreciable core to rim zoning patterns (Figure 5a, b). Specifically, the patterns in Figure 5 display: (i) an increase in X_{Gr} from the inner core (0.48–0.50) towards its outer part (0.52–0.54) (Figures 5a, b), and constant values of ~0.54 in the rim (Figure 5a, b); (ii) an increase in X_{Alm} from the core (0.20–0.23) towards rim (0.32–0.36) (Figures 5a, b), where in some cases remains constant (Figure 5b); (iii) a roughly bell-shaped zoning pattern in X_{Sps} (Figures 5a, b), with values of 0.20–0.24 in the core and 0.09–0.10 in the outermost part of the rim. Both the X_{Andr} (calculated as [2 - ($Al_{a.p.f.u.}$ + $Ti_{a.p.f.u.}$ + $Cr_{a.p.f.u.}$)] in the Y site) and X_{Py} core–rim trends are below 0.10 mole fractions (Figure 5b), and are respectively characterised by: (i) almost constant values from the inner core towards the rim (~0.05), and (ii) increasing values from the core (~0.00) towards the outermost part of the rim (~0.01).

White mica is mostly fine-grained (up to ~50 μm in size) and aligned along the main mylonitic foliation S_m (Figures 4d, e), where it overgrows the relict biotite flakes (Figure 4e). It is enriched in the ferro-celadonite end-member with Si = 3.32–3.39 apfu and X_{Fe} = 0.59–0.69 (Table 2) with respect to the larger muscovite flakes (up to ~300μm in size), which have Si ≈ 3.05 apfu and X_{Fe} ≈ 0.59 (Table S2). Subhedral to euhedral grains of epidote have been observed in the mica-rich layers either aligned along the main mylonitic foliation S_m (Figure 4d, e) or around small garnet grains (Figure 5b). The epidote has ~2.45 apfu of Al and ~0.51 apfu of Fe^{3+} (Table 3). Sphene is characterised by ~0.16 apfu of Al and ~0.02 apfu of Fe^{3+} (Table 3), and occurs in large coronae (up to ~100 μm) around ilmenite as well as in small euhedral grains within the mica-rich layers (Figure 4d). Moreover, sphene showing micro-inclusions of ilmenite is also found to be occasionally hosted within garnets (Figure 4f, top right inset).

3.3.2 Sample VF79GR

Sample VF79GR is a garnet-bearing, biotite-free mylonitic leucocratic orthogneiss (Figures 3e, f) with K-feldspar and quartz porphyroclasts within a fine-grained quartzofeldspathic matrix, which sporadically alternates with very thin white mica layers (Figure 4g). The mineral assemblage of sample VF79GR is composed of quartz + K-feldspar + plagioclase + white mica + garnet + epidote + sphene. K-feldspar, quartz and albite (X_{An} ~0.01) (Table 2) comprise the fine-grained recrystallised matrix (Figures 4g, h). Garnets (up to ~250 μm in size) are wrapped by the main mylonitic foliation (Figure 4h), and have grossular-rich compositions (Table 4) that exhibit very similar end-members' zoning patterns from core to rim as those of the garnets from sample VF77GR (Figures 5c, d). In particular, the patterns in Figure 5 are characterised by: (i) a general increase in X_{Gr} from ~0.45 to 0.50–0.54 from the inner core to its outer part (Figures 5c, d, especially 5c), and almost constant values of ~0.53 and/or ~0.50 in the rim (Figures 5c, d); (ii) an increase in X_{Alm} from the inner core (0.23–0.28) towards the outer part (0.30–0.32) (Figures 5c, d), and lower (~0.27) but roughly constant values in the rim; (iii) a gentle decrease in X_{Sps} (Figure 5c) from 0.20–0.22 in the inner core to 0.15–0.16 in the outer core, which is followed by nearly constant values in the rim and an eventual drop to 0.12–0.14. The core–rim trend in X_{Andr} is best highlighted in Figure 5c, which reveals: (i) variations in the core from ~0.03 to ~0.11 mole fractions followed by a decreasing trend up to plateau at ~0.06 mole fractions in the rim. On the other hand, the X_{Py} maintains at around zero mole fractions throughout the traverses (Figures 5c, d).

The white mica is fine-grained (up to ~30 μm in size), aligned along the main mylonitic foliation (Figure 4g) and enriched in the ferro-celadonite end-member (Si_{apfu} = 3.34–3.38 and X_{Fe} = 0.66–0.68; similar to sample VF77GR) (Table 2) with respect to the few, larger muscovite flakes (Figure 4g) that show Si = 3.09–3.14 apfu and X_{Fe} = 0.57–0.59 (Table S2). Epidote is widespread in the rock matrix and has a sub-euhedral to euhedral shape. It is characterised by ~2.36 apfu of Al and ~0.59 apfu of Fe^{3+} (Table 3). Sphene is present as small euhedral grains within the rock matrix, with ~0.29 apfu of Al and ~0.01 apfu of Fe^{3+}, respectively (Table 3).

4 PHASE EQUILIBRIUM MODELLING

4.1 Models and modelling strategy

Phase equilibrium diagrams have been calculated using the THERMOCALC v3.45 software (Powell & Holland, 1988) with the updated version of the Holland & Powell (2011) dataset (file tc-ds63.txt, created on 05/01/2015). The used activity–composition models are: clinopyroxene (Green et al., 2016); garnet, biotite, muscovite, paragonite, margarite, cordierite, orthopyroxene, chlorite and ilmenite (White, Powell, & Johnson, 2014); epidote (Holland & Powell, 2011) and feldspars (Holland & Powell, 2003). The quartz, albite, sphene, rutile, kyanite, sillimanite, andalusite, and aqueous fluid end-members have been assumed to be pure phases. The bulk rock compositions have been converted from weight percentages (wt.%) to mole percentages (mol%) in the MnNCKFMASHTO 11-component model system (Table 5). The modelled mole percentages of CaO have been reduced on the basis of the P_2O_5 content, due to the presence of apatite. To determine the appropriate Fe^{3+}/Fe_{tot} ratio in samples VF80GR, VF77GR, and VF79GR, *P*–*X*$(Fe)^{3+}$ isothermal phase diagrams have been calculated at 500 °C for each sample (Figure S1). Such temperature was chosen to investigate the mineral assemblages forming at the greenschist–amphibolite facies transition with respect to the Alpine *P*–*T* conditions obtained by Langone et al. (2006) (*P* = 0.75–0.90 GPa and *T* = 525±50°C) for the mylonitic orthogneiss of the Castagna Unit. Hence, the $X(Fe)^{3+}$ used in the phase diagrams of Figures 6–9 was selected within the opportune stability fields, i.e., at $X(Fe)^{3+}$ lower than that favouring hematite stabilisation for the weakly-deformed orthogneiss (Figure S1), and at $X(Fe)^{3+}$ in the centre of the g + mu + bi + ep + ab + q + ksp + sph stability field for the mylonitic orthogneisses (Figure S1).

4.2 Principal reactions producing HP-mineral assemblages

The mineral assemblages that developed in the weakly-deformed orthogneiss (sample VF80GR) and mylonitic orthogneisses (samples VF77GR and VF79GR) during the main tectono-metamorphic events are summarised in Table 6. In sample VF80GR, the presence of subhedral epidote crystals together with tiny white mica overgrowths on large biotite flakes (Figures 4a, b), suggest the consumption of aqueous fluid within the simplified CKASH and KMASH systems, respectively:

anorthite + K-feldspar + H_2O = clinozoisite + muscovite + quartz, (1)

K-feldspar + phlogopite + quartz + H_2O = celadonite. (2)

Equilibria (1) and (2) highlight the fluid (H_2O) demand required to stabilise the clinozoisite and celadonite end-members of the epidote and white mica, respectively. Moreover, the sphene coronae around ilmenite in sample VF80GR (Figure 4c) may have formed in response to hydration reactions as that in the following CKFASHT system:

anorthite + ilmenite + K-feldspar + H_2O = muscovite + annite + sphene + quartz. (3)

Accordingly, Harlov, Tropper, Seifert, Nijland, & Förster (2006) demonstrated that ilmenite replacement by sphene is not solely a function of the *P*–*T* conditions as previously believed (e.g. Enami, Suzuki, Liou, & Bird, 1993), but may be strongly influenced by changes in fH_2O and/or fO_2.

Within the mylonitic orthogneisses (sample VF77GR and VF79GR), the microstructural relationships evidence the overgrowth of tiny ferro-celadonite-rich white-mica on large biotite flakes and the overgrowth of sphene on relict ilmenite (Figure 4e), as also recorded in the weakly-deformed orthogneiss. This mineral paragenesis is consistent with the fluid consumption, as evidenced from equilibria 2 and 3. In addition, grossular-rich garnets (Table 4) occur in the mylonitic orthogneisses (Figure 4e, h), as the main mineral phase indicative of the prograde metamorphism. These garnets host tiny quartz, albite, and white mica inclusions (Figure 5) as well as sphene coronae around ilmenite remnants (Figure 4f), thus suggesting that garnet started to grow when these minerals were already present. According to the petrographic evidences, the stabilisation of grossular-rich garnet cores in the investigated mylonitic orthogneisses may have primarily occurred, via the following hydration reaction in the simplified CKASH system:

anorthite + K-feldspar + H_2O = grossular + muscovite + quartz. (4)

Equilibrium (4) evidences the linkage between the stabilisation of the Ca-rich garnet (Table 4) and the availability of fluid in the system. However, biotite was also involved in the stabilisation of garnet in mylonitic samples, providing Fe and Mn through equilibria (5) and (6):

muscovite + annite + quartz = almandine + K-feldspar + H_2O, (5)

muscovite + Mn-biotite + quartz = spessartine + K-feldspar + H_2O. (6)

Equilibria 4–6 imply the consumption and release of fluid respectively, potentially suggesting H_2O-conservation during the garnet stabilisation. Accordingly, it can be inferred that biotite may have been part of the mineral assemblage at least up to the peak metamorphic conditions, when it was either nearly (sample VF77GR) or completely (sample VF79GR) consumed as metamorphism progressed (Table 6). Around garnet and biotite, a further ferro-celadonite-rich white mica grew along the mylonitic foliation (Figure 4d, h), as indicative of the last metamorphic stage (Table 6). Therefore, the succession of the mineral assemblages in the weakly- to mylonitic orthogneisses was related to both hydration (i.e. equilibria 1–4) and dehydration reactions (i.e. equilibria 5–6); hence, the phase equilibrium modelling is focused to the investigation of the fluid-present and fluid-deficient conditions when the former celadonite-rich white mica (produced by equilibrium 1), epidote, sphene, garnet and the ferro-celadonite-rich white mica were stabilised.

4.3 Post-Hercynian hydration in the weakly-deformed orthogneiss

The occurrence of new epidote grains (Figure 4a) and sphene coronae (Figure 4c) in the weakly-deformed orthogneiss (sample VF80GR) is explored in Figure 6a. A P–M_{H2O} pseudosection has been calculated near the greenschist–amphibolite facies transition in the pressure range of 0.2–1.4 GPa and at a constant temperature of 500 °C. At this temperature, the mineral assemblage pl + bi + mu + ab (+q + ksp), where oligoclase and albite occur together at the peristerite solvus, is either H2O-saturated for M(H_2O) > 4.0 mol% if rutile is stable, or H_2O-undersaturated if ilmenite is stable (assemblage 1 in Figure 6a) for ~3.6 mol% of H_2O bound in OH-bearing minerals, i.e., biotite and muscovite in this case. Although the stability of rutile and/or ilmenite is dependent on the oxidation state, ilmenite was observed in the studied rocks (Figure 4) while rutile was not detected (cf. Table 6). Therefore, moving at a constant 3.6 mol% of H_2O towards a higher pressure in the phase diagram (e.g., assemblage 12 in Figure 6a), epidote and sphene never stabilise in the mineral assemblages encountered. Indeed, to stabilise these phases, a higher fluid content in the bulk rock of approximately 4.9 H_2O mol% (assemblage 2 in Figure 6a) is required.

To investigate the changes that can occur in the equilibrium mineral assemblages within the *P*–*T* space when fluid is added to the rock, two *P*–*T* pseudosections have been calculated for the bulk rock compositions of the mineral assemblages 1 (ksp-pl-bi-mu-ab-ilm-q) and 2 (ep-ksp-pl-bi-mu-ab-sph-q) (Figures 6b, c), whose difference is the previously inferred H_2O content (i.e., 3.6 mol% and 4.9 mol%). The mineral assemblage (1) exhibits an upper pressure limit of ~0.45 GPa for a temperature ranging from 470 to 550 °C, under H_2O-undersaturated conditions (Figure 6b). This mineral assemblage appears to have formed on a primary pl (oligoclase) + bi + mu + ilm + H_2O (+ q + ksp) paragenesis, which is stable at low-*P* amphibolite facies conditions from ~640 °C (Figure 6b), and seems to correspond to the late-Hercynian metamorphic conditions (e.g. Ortolano et al., 2020). The *P*–*T* stability field of the mineral assemblage (2) is composed of ep + pl (oligoclase) + bi + mu + ab + sph (+q + ksp), and is shown in the *P*–*T* pseudosection in Figure 6c, which is calculated by considering 4.9 mol% of H_2O. Noticeably, Figure 6c reveals that the new mineral assemblage is stable in a *P* range of 0.2–1.0 GPa and *T* range of 390–590 °C, which covers H_2O-undersaturated and H_2O-saturated conditions (Figure 6c).

4.4 Alpine peak metamorphic conditions in mylonitic orthogneisses

Alpine peak metamorphic conditions have been firstly investigated in sample VF77GR (mylonitic orthogneiss) and then in sample VF79GR (mylonitic leucocratic orthogneiss), moving towards the contact with the Sila and Serre Unit along the transect in Figure 2. To reproduce the garnet zoning patterns, equilibria in these rocks have been modelled by considering (i) fully H_2O-saturated conditions (i.e. H_2O set in excess) and (ii) partly H_2O-saturated conditions (Table 5).

4.4.1 Sample VF77GR: equilibria under fully H_2O-saturated conditions

The case of complete rehydration of the relict metamorphic mineral assemblage during Alpine tectonics has been investigated by calculating a *P*–*T* phase diagram with fluid (H_2O) set in excess (Figure 7a). Under H_2O-saturated conditions, garnet is present in the observed q + ksp + ab + g + ep + mu + bi + sph mineral assemblage from a minimum pressure of ~0.6 GPa, with the upper stability field of this assemblage limited at higher pressure by the diopside-in curve. To

reproduce the core–rim compositional variation for the garnet (Figures 5a, b), the X_{Gr} and X_{Sps} isopleths have been plotted in Figure 7b. The X_{Gr} isopleths can be reproduced between the lowest (0.48) and highest (0.54) molar fractions (Figures 5a, b), whereas the lowest reproducible X_{Sps} molar fraction is 0.12 (Figure 7b). The composition isopleths in Figure 7b suitably represent the growth of the garnets' core (i.e. X_{Sps} of 0.24–0.20 and X_{Gr} of 0.48–0.52 in Figures 5a, b) as well as the rim compositions of some garnets (i.e. X_{Sps} of 0.14–0.16 and X_{Gr} of 0.52–0.54 in Figure 5a). The phase diagram in Figure 7b clearly shows that garnet grew at conditions of ~0.75 GPa and 540 °C up to ~0.96 GPa and 590 °C, in the g + ep + bi + mu + ab + sph (+q + ksp) stability field, if H_2O saturation is assumed. The maximum *P*–*T* conditions are recorded either in the latter part of the rim of some garnets (Figure 5a) or in the outer core of some other crystals (X_{Sps} of ~0.12 and X_{Gr} of ~0.54), as illustrated in Figure 5b.

The main outcome of modelling the mylonitic orthogneiss (sample VF77GR) with excess fluid is the irreproducibility of X_{Sps} values lower than 0.12 molar fraction, which are recorded in in the rim of some garnets (Figure 5b). Therefore, fully H_2O-saturated conditions do not completely satisfy the composition of growing garnet.

4.4.2 Sample VF77GR: equilibria under partly H_2O-saturated conditions

Excluding the fully H_2O-saturated conditions, phase equilibria in sample VF77GR were also investigated under variable degrees of hydration to reproduce the zoning patterns of the garnet in the same mylonitic orthogneiss. The first modelled amount of H_2O, was that required to saturate the wet solidus at 1.2 GPa and 620 °C (i.e. 3.31 mol% of H_2O), with quartz and K-feldspar present in all fields. This H_2O content reproduces H_2O-saturated conditions for the stability field of the observed g + ep + bi + mu + ab + sph (+q + ksp) mineral assemblage (Figure 8a), with an amount of fluid that is different (lower) from that modelled in Figure 7. Accordingly, both the phase diagrams of Figure 7a and 8a were calculated for the same sample, but the different amounts of H_2O make them not completely identical. For instance, the *LP* tip of the g-ep-bi-mu-ab-sph stability field is at ~0.65 GPa and ~540°C in Figure 7a, whereas it is at ~0.55 GPa and ~515°C in Figure 8a, making this P–T stability field in Figure 8a wider than in Figure 7a. However, the reproducible X_{Sps} isopleths of the garnet are the same as those in Figure

7b, and the garnet rim composition in Figure 5b is thus irreproducible, with the intersection in the outer part of the core (X_{Gr} = 0.52 and X_{Sps} = 0.12) occurring again at ~0.96 GPa and ~590 °C. The Si_{apfu} isopleth is strongly affected by the fluid availability in the system; it runs parallel to the H_2O-saturation curve and does not exhibit any reliable intersection with the X_{Gr} and X_{Sps} of the garnet (Figure 8b). To investigate the growth of garnet rims in relation to dehydration during the prograde path, the H_2O-mode isopleths were contoured (Figure 8b). This contouring highlights how the H_2O content of the rock does not vary during the growth of the garnet's core within the g + ep + bi + mu + ab + sph + H_2O stability field (Figure 8b). This testifies that garnet formed while the rock was following a steep prograde path where the fluid, provided by devolatilization reactions (e.g. equilibria 5–6), was almost stored within simultaneously forming OH-bearing minerals like white mica (e.g. equilibrium 2).

To investigate if the evolutionary path of the mylonitic orthogneiss of the Castagna Unit was characterised by fluid-deficient conditions, a T–M_{H2O} pseudosection was calculated at a constant P of 0.96 GPa by varying the H_2O mol% from 3.31 to 0.00 (Figure 8c). This isobaric phase diagram shows that the outermost rim compositions of garnet (i.e. X_{Gr} = 0.54 and X_{Sps} = 0.09) are reproduced in the di + g + ep + bi + mu + ab + sph stability field under H_2O-deficient conditions of 2.81 mol% of H_2O bound within OH-bearing minerals, at a T of < 590 °C. Consequently, a P–T pseudosection was calculated considering the fluid content equal to 2.81 mol% (Figure 8d). The intersections between the X_{Sps} and X_{Gr} isopleths of the garnet, together with the slope of the H_2O-saturated curve, setting the H_2O-conservative character, indicate that the prograde path occurred from 0.70–0.75 GPa and 540–545 °C (X_{Gr} = 0.48 and X_{Sps} = 0.22) up to the metamorphic peak at ~0.96 GPa and ~590 °C (X_{Gr} = 0.52 and X_{Sps} = 0.12). The composition of the outermost rim of the garnets (X_{Gr} = 0.54 and X_{Sps} = 0.09), suggests that probably, retrogression with nearly isobaric cooling, down to ~540 °C, resulted under H_2O-undersaturated conditions.

4.5 Sample VF79GR: metamorphic peak and post-peak exhumation under fluid-present conditions

As reported so far, garnet is progressively stabilised and the modal abundance of biotite progressively decrease (Figures 2 and 3) when moving from the weakly-deformed orthogneiss (sample VF80GR) towards the garnet-bearing, biotite-free mylonitic leucocratic orthogneiss (sample VF79GR). These variations are evident in the T–X_{bulk} pseudosection in Figure 9a, calculated at 0.95 GPa from sample VF80GR to sample VF79GR, assuming for both samples 4.9 mol% of H_2O bound within OH-bearing minerals (see Table 5). In this phase diagram the expansion of the garnet stability field (cf. assemblages 1 and 3 at T < 600 °C, and assemblages 4 and 6 at T > 600 °C) as well as the decrease of the biotite mode are illustrated. Accordingly, this isobaric phase diagram highlights the control of the bulk rock composition on mineral assemblages as well as how fluid-present conditions are favoured in mylonitic metagranitoids with lower FeO_t, MgO and TiO_2 and higher K_2O contents (cf. Table 1, samples VF80GR and VF79GR). The calculated equilibria at 0.95 GPa for X_{bulk} = 1 in Figure 9a, support the interpretation that the mylonitic leucocratic orthogneiss (sample VF79GR) is H_2O-undersaturated at a T < 510 °C for the fluid content considered. This results in small amounts of biotite expected to be stable in this rock under peak-pressure conditions, even at T of < 510 °C, which seems not corresponding to the absence of biotite within this rock (cf. Table 6). Therefore, since the equilibria consuming biotite require the presence of fluid, the phase equilibria considering a higher fluid content (i.e., 6.5 mol%; Table 5) are explored in the phase diagram in Figure 9b. Here, for this fluid content the biotite-free mylonitic mineral assemblage of sample VF79GR (cf. Table 6) is reproduced at P of 0.6–0.7 GPa and T of 360–400 °C during retrogression: this is suggested by the contouring of composition isopleths of X_{Sps} and X_{Gr} of garnet in Figure 9c showing that garnet growth started in the bi-stability field at P of 0.70–0.76 GPa and T of 530–560 °C (X_{Sps} = 0.20–0.22 and X_{Gr} = 0.46–0.50 of garnet cores, cf. Figures 5c, d) up to peak metamorphic conditions of 0.88–0.94 GPa and 560–590 °C (X_{Sps} = 0.12–0.14 and X_{Gr} = 0.50–0.54 of garnet outermost rims, cf. Figures 5c, d). The contouring of Si in muscovite, together with the disappearance of biotite, highlight how the tiny recrystallised ferro-celadonite-rich white mica, having Si up to 3.38 apfu in sample VF79GR (Table 2), record the P–T conditions of equilibration during retrogression around 0.6–0.7 GPa and 350–400 °C, before entering the g+ep+mu+ab+sph (+q+ksp+H_2O) stability field (Figure 9c). Noticeably,

while the Si content of white mica is *P*-sensitive in biotite-bearing mineral assemblages, it becomes *T*-sensitive in biotite-free mineral assemblages (Figure 9c).

5 DISCUSSION

The following discussion is focused on: (i) the Alpine *P–T–fluid* evolution experienced by the orthogneisses of the Castagna Unit, and (ii) some general considerations regarding the evolution of the CGL during Alpine orogeny.

5.1 Alpine *P–T–fluid* evolution of the orthogneisses

The modelling results are summarised in Figure 10a, where the *P–T* stability field of the weakly-deformed orthogneiss (VF80GR) and the *P–T–fluid* paths of the mylonitic orthogneisses (VF77GR, VF79GR) are shown together. In particular, the stability field of the ep-pl-bi-mu-ab-q-ksp-sph mineral assemblage of the weakly-deformed orthogneiss (from Figure 6c) is reported in Figure 10a. This mineral assemblage, formed under conditions where hydration occurred but in insufficient degrees to saturate the assemblage, allowing the stabilisation of epidote and sphene at the expense of an inherited, late-Hercynian metamorphic mineral paragenesis (i.e. pl-bi-mu-q-ksp-ilm in Figure 6b). On the whole, the *P–T* space of the ep-pl-bi-mu-ab-q-ksp-sph mineral assemblage has an upper pressure limit of ~1.0 GPa and a *T* range of ~420–600 °C (Figure 10a). As regards the mylonitic orthogneisses (sample VF77GR and VF79GR), the modelling results show that garnet started to grow under H_2O-saturated conditions (Figures 7–9). These garnets, which host quartz, albite, muscovite, and sphene inclusions record the prograde path, up to peak metamorphic conditions of ~0.9–1.0 GPa and ~590 °C (Figures 7–9), within their core to rim zoning patterns (Figure 5a). Moreover, some of the garnets in sample VF77GR (Figure 5b) show rim-equilibration in the *T* range of 540–590 °C at peak pressure conditions of ~0.96 GPa, under fluid-deficient conditions (Figures 8, 10a). Although the thermobarometric results obtained from intersections of garnet compositional isopleths have to be cautiously considered given the uncertainties related to the small core–rim differences in X_{Gr} values, along with the poorly constrained behaviour of Mn in many minerals, some general considerations on the obtained prograde *P–T* evolution and the *P–T* stability field

of mineral assemblages can be however made. In fact, the prograde path obtained by modelling the garnet zoning patterns in mylonitic orthogneiss roughly overlaps the stability field of the mineral assemblage in the weakly-deformed orthogneiss, as illustrated in Figure 10a. Accordingly, it is possible to deduce that the whole orthogneiss body of the Castagna Unit shared the same peak metamorphic conditions under a geothermal gradient of ~16–17 °C/km (assuming a granitic crust density of 2750 kg/m^3) (Figure 10a). Moreover, within the mylonitic orthogneisses, biotite is less abundant than in the weakly-deformed orthogneiss or it is completely absent, as in the case of sample VF79GR, because replaced by tiny, ferro-celadonite-rich white mica (Table 2). This tiny white mica, which defines the main mylonitic foliation (Figure 4), records, in sample VF79GR, equilibration under H_2O-saturated conditions near the biotite-out curve, in proximity to the g-ep-mu-ab-q-ksp-sph mylonitic mineral assemblage (Figure 9c). The *P*–*T* space of equilibration of this mineral assemblage is 0.6–0.7 GPa and 360–400 °C, and allows the definition of the exhumation and cooling trajectory followed by the Castagna Unit mylonitic orthogneisses, along with the resulting anticlockwise shape of the *P*–*T* path (Figure 10a). Comparing our results with the thermobarometric estimates by Langone et al. (2006) on orthogneisses of the Castagna Unit, the *P*–*T* estimates by these authors suitably overlap along the exhumation and cooling path obtained in this study (Figure 10b).

Analysing the obtained *P*–*T* paths with respect to the fluid-present/deficient conditions from the weakly-deformed to the mylonitic orthogneisses (Figure 10a), it can be argued that the hydration event that favoured the stabilisation of the new Alpine mineral assemblages in these rocks, probably occurred during the rifting phase preceding the Alpine compressive tectonics in Calabria (e.g. Liberi et al., 2011). In fact, as demonstrated in other case studies of prograde ductile shear zones set in metagranitoids rocks (e.g. Leydier, Goncalves, Lanari, & Oliot, 2019), an aqueous fluid could have infiltrated along planar discontinuities (e.g. old schistosity planes) and/or brittle structures (e.g. fractures) before the onset of Alpine tectonics, with resulting fluid-present conditions in the orthogneisses when under-thrusting of the Castagna Unit below the Sila and Serre Unit commenced (Figure 10b). Successively, during the Eocene compressive tectonics, the Castagna Unit experienced burial and thrusting below the Sila and Serre Unit

(Festa et al., 2020) (Figure 10b). The interpreted *P*–*T* evolution for the Castagna Unit mylonitic orthogneisses shown in Figure 10a, evidences that H_2O-saturated conditions characterised the prograde path of these rocks up to the Alpine metamorphic peak (*P* of ~0.9–1.0 GPa and *T* of ~590 °C) at *c*. 43 Ma (Schenk, 1990). These peak conditions were reached following an almost H_2O-conservative trajectory (Figure 8), which resulted from the simultaneously operating reactions of devolatilization, due to biotite breakdown to form garnet (e.g. equilibrium 5), and of fluid-consumption, to form the celadonite rich white mica (e.g. equilibrium 2). Hence, it can be deduced that the stabilisation of garnet in the mylonitic orthogneisses, rather than in the weakly-deformed orthogneiss, was aided by the fluid-present conditions (Figure 8, 9) which likely exerted a catalytic role to mineral stabilisation (e.g. Rubie, 1986). After the cessation of under-thrusting, the Castagna Unit mylonitic orthogneisses experienced cooling at high-*P* conditions (Figure 10a). This is recorded in the rim compositions of some garnets from sample VF77GR, which evidence equilibration in H_2O-undersaturated conditions during isobaric cooling at a *P* of ~0.9–1.0 GPa (Figure 10a). On the other hand, closer to the tectonic contact with the Sila and Serre Unit, the prograde to retrograde path of the mylonitic leucocratic orthogneiss (sample VF79GR) is H_2O-saturated, as recorded in the core to rim compositions of the garnets and by the Si contents of the tiny white micas, respectively (Figure 9, 10a). Therefore, it can be inferred that the remaining fluid in the mylonitic orthogneisses, was channelled towards the tectonic contact with the Sila and Serre Unit after the peak metamorphic conditions were reached, promoting fluid-present conditions in these rocks (Figure 10b) during the exhumation.

5.2 Evolution of the CGL during Alpine orogeny

About the *P*–*T* path obtained, some final considerations on (i) the location of the CGL during the Eocene compressive tectonics with respect to the Alpine subduction, and (ii) the re-activation of the CGL during the Oligocene–Miocene extensional tectonics in Calabria, can be outlined. The prograde part of the modelled path indicates stacking of the Calabria continental crust during Eocene Alpine compressive tectonics (Festa et al., 2020), with the Castagna Unit orthogneiss, under-thrusting the Sila and Serre Unit, that reached a depth of ~35 km under a

geothermal gradient of ~16–17 °C/km. After the cessation of under-thrusting, the peculiar isobaric cooling trajectory, under HP conditions (Figure 10b), indicates that the orthogneisses of the Castagna Unit started to experience cooling at high-P conditions. Rocks that experienced this type of *P*–*T* evolution were interpreted by Wakabayashi (2004) and Willner, Glodny, Gerya, Godoy, & Massonne (2004) as recording involvement in the subduction process. Accordingly, it can be argued that the location of the CGL was in proximity to the cold subducting Ligurian Tethys' oceanic crust (Tursi, Bianco, et al., 2020), which promoted deflection of the isotherms in the obducting continental crust, and cooling, under *HP* conditions, in the Castagna Unit orthogneiss. This is also corroborated by the general cold character of the Alpine subduction zone in Calabria, where a geothermal gradient of ~6.6 °C/km at peak metamorphic conditions, was obtained by Tursi, Bianco, et al. (2020) for the lawsonite-clinopyroxene blueschists of the oceanic crust subducting beneath the continental margin.

The subsequent exhumation and cooling of the orthogneisses of the Castagna Unit to 0.6–0.7 GPa and 360–400 °C can be suitably reconciled with the evolutionary structural model for the CGL by Festa et al. (2020). According to this model, exhumation of the Castagna Unit's orthogneisses happened during ductile re-activation of the CGL under an extensional regime that likely occurred during (late Eocene?) Oligocene to early Miocene. This tectonic re-activation is thereby supported by the microstructural evidence presented in this study, where the tiny, syn-kinematic ferro-celadonitic white mica defines the main mylonitic foliation and shows equilibration in the retrograde path (e.g. Figure 9c, 10b). In addition, sphene in mylonitic orthogneisses, together with the modelled Ca-rich garnets (e.g. Figure 4), show equilibration during the prograde stage of metamorphism related to under-thrusting (Figure 10b), providing constraints for the extensional re-activation of the former compressive Curinga–Girifalco Line. The preservation of the prograde history of the Castagna Unit orthogneiss, along with the anticlockwise shape of the *P*–*T* trajectory, were therefore possible since no high-*T* overprint occurred during exhumation of these rocks (i.e. no Alpine magmatism is recorded in Calabria), which is the main factor for erasing these information (e.g. Wakabayashi, 2004).

6 CONCLUSIONS

The present study provides the first reconstruction of the Alpine *P–T–fluid* evolution experienced by the orthogneisses of the Castagna Unit in Calabria, along with the useful information that can be retrieved from forward thermodynamic modelling of metagranitoids relating their mineral parageneses with respect to fluid-present/-deficient conditions during metamorphism. The results showed that the Castagna Unit was first subjected to hydration during the rifting phase preceding the Alpine compressive tectonics in Calabria. During the Alpine orogeny, the Castagna Unit's orthogneisses experienced under-thrusting to lower crust depths along the CGL, with the mineral assemblage of these rocks varying in relation to the distance from the Sila and Serre Unit. Accordingly, the *P–T* evolutionary path of the mylonitic orthogneisses was either characterised by transient H_2O-saturated and H_2O-undersaturated conditions, far from the tectonic contact, or persistent H_2O-saturated conditions close to the contact. These *P–T–fluid* conditions were primarily recorded in the core–rim composition of garnet and also in recrystallised phengitic white micas. The obtained paths, evidence under-thrusting in a "closed system" along a fluid-conservative trajectory, up to the peak metamorphic conditions of ~0.9–1.0 GPa and ~560–590 °C. Different degrees of fluid saturation affected the post-peak evolution of the mylonitic orthogneisses. Accordingly, isobaric cooling in H_2O-undersaturated conditions is recorded in mylonitic orthogneisses far from the tectonic contact, whereas H_2O-saturated conditions affected the mylonitic orthogneisses close to this contact. This resulted from the channelling, within the shear zone, of the fluid towards the tectonic contact with the Sila and Serre Unit during re-activation, under an extensional regime, of the previously compressive shear zone. The overall anticlockwise *P–T* evolution recorded by the Castagna Unit mylonitic orthogneisses thus evidence the involvement of this tectono-metamorphic unit into the Eocene subduction process in Calabria.

ACKNOWLEDGEMENTS

We are grateful to Simon Harley and Richard W. White for their careful editorial handling. Pavel Pitra, Simon Schorn and two anonymous reviewers are thanked for their constructive criticism. FT thanks the University of Bari Aldo Moro for the PhD grant in Geosciences. The authors are grateful to Nicola Mongelli for assistance during the SEM-BSE sessions.

References

Acquafredda, P., Lorenzoni, S., & Zanettin Lorenzoni, E. (1994). Paleozoic sequences and evolution of the Calabrian Peloritani Arc (Southern Italy). *Terra Nova*, *6*, 582–594.

Altenberger, U., Prosser, G., Grande, A., Günter, C., & Langone, A. (2013). A seismogenic zone in the deep crust indicated by pseudotachylytes and ultramylonites in granulite-facies rocks of Calabria (Southern Italy). *Contributions to Mineralogy and Petrology*, *166*(4), 975–994. https://doi.org/10.1007/s00410-013-0904-3

Altenberger, U., Prosser, G., Ruggiero, M., & Günter, C. (2011). Microstructure and petrology of a Calabrian garnet-bearing pseudotachylyte – a link to lower-crustal seismicity. *Geological Society, London, Special Publications*, *359*(1), 153–168. https://doi.org/10.1144/SP359.9

Amodio-Morelli, L., Bonardi, G., Colonna, V., Dietrich, D., Giunta, G., Ippolito, F., … Zuppetta, A. (1976). L'Arco Calabro-Peloritano nell'Orogene Appenninico-Maghrebide. *Memorie Della Società Geologica Italiana*, *17*, 1–60.

Angì, G., Cirrincione, R., Fazio, E., Fiannacca, P., Ortolano, G., & Pezzino, A. (2010). Metamorphic evolution of preserved Hercynian crustal section in the Serre Massif (Calabria–Peloritani Orogen, southern Italy). *Lithos*, *115*(1–4), 237–262. https://doi.org/10.1016/j.lithos.2009.12.008

Argles, T. W., Prince, C. I., Foster, G. L., & Vance, D. (1999). New garnets for old? Cautionary tales from young mountain belts. *Earth and Planetary Science Letters*, *172*(3–4), 301–309. https://doi.org/10.1016/S0012-821X(99)00209-5

Bell, T. H., & Hayward, N. (1991). Episodic metamorphic reactions during orogenesis: the control of deformation partitioning on reaction sites and reaction duration. *Journal of Metamorphic Geology*, *9*(5), 619–640. https://doi.org/10.1111/j.1525-1314.1991.tb00552.x

Biino, G., & Compagnoni, R. (1992). Very-high pressure metamorphism of the Brossasco coronite metagranite, southern Dora Maira Massif, Western Alps. *Schweizerische Mineralogische Und Petrographische Mitteilungen*, *72*(3), 347–363.

Bonardi, G., Cavazza, W., Perrone, V., & Rossi, S. (2001). Calabria-Peloritani terrane and northern Ionian Sea. In *Anatomy of an Orogen: the Apennines and Adjacent Mediterranean Basins* (pp. 287–306). Dutch, The Netherlands: Springer.

https://doi.org/10.1007/978-94-015-9829-3_17

Brandt, S., & Schenk, V. (2020). Metamorphic response to Alpine thrusting of a crustal-scale basement nappe in southern Calabria (Italy). *Journal of Petrology*. https://doi.org/10.1093/petrology/egaa063

Bruno, M., Compagnoni, R., & Rubbo, M. (2001). The ultra-high pressure coronitic and pseudomorphous reactions in a metagranodiorite from the Brossasco-Isasca Unit, Dora-Maira Massif, Western Italian Alps: A petrographic study and equilibrium thermodynamic modelling. *Journal of Metamorphic Geology*, *19*(1), 33–43. https://doi.org/10.1046/j.1525-1314.2001.00291.x

Caggianelli, A., Prosser, G., Festa, V., Langone, A., & Spiess, R. (2013). From the upper to the lower continental crust exposed in Calabria. *Geological Field Trips*, *5*(1.2), 1–49. https://doi.org/10.3301/GFT.2013.02

Caggianelli, A., Prosser, G., & Rottura, A. (2000). Thermal history vs. fabric anisotropy in granitoids emplaced at different crustal levels: An example from Calabria, Southern Italy. *Terra Nova*, *12*(2), 109–116. https://doi.org/10.1111/j.1365-3121.2000.00280.x

Carminati, E., & Doglioni, C. (2012). Alps vs. Apennines: The paradigm of a tectonically asymmetric Earth. *Earth-Science Reviews*, *112*(1–2), 67–96. https://doi.org/10.1016/j.earscirev.2012.02.004

Carswell, D. A., Wilson, R. N., & Zhai, M. (2000). Metamorphic evolution, mineral chemistry and thermobarometry of schists and orthogneisses hosting ultra-high pressure eclogites in the Dabieshan of central China. *Lithos*, *52*(1–4), 121–155. https://doi.org/10.1016/S0024-4937(99)00088-2

Cirrincione, R., Ortolano, G., Pezzino, A., & Punturo, R. (2008). Poly-orogenic multi-stage metamorphic evolution inferred via P-T pseudosections: An example from Aspromonte Massif basement rocks (Southern Calabria, Italy). *Lithos*, *103*(3–4), 466–502. https://doi.org/10.1016/j.lithos.2007.11.001

Colonna, V. (1998). Ruolo ed estensione regionale dei thrusts a vergenza settentrionale in Sila Grande (Calabria). *Bollettino Della Società Geologica Italiana*, *117*(1), 249–260.

Colonna, V., & Piccarreta, G. (1975). Schema strutturale della Sila Piccola. *Bollettino Della Societa Geologica Italiana*.

Compagnoni, R., & Rolfo, F. (2003). UHPM units in the Western Alps. In *EMU Notes in*

Mineralogy (pp. 13–49). https://doi.org/10.1180/emu-notes.5.2

Enami, M., Suzuki, K., Liou, J. G., & Bird, D. K. (1993). Al-Fe3+ and F-OH substitutions in titanite and constraints on their P-T dependence. *European Journal of Mineralogy*. https://doi.org/10.1127/ejm/5/2/0219

Etheridge, M. a, Wall, V. J., & Vernon, R. H. (1983). The rule of fluid phase during regional metamorphism and deformation. *Journal of Metamorphic Geology*, *1*, 205–236.

Festa, V., Caggianelli, A., Langone, A., & Prosser, G. (2013). Time–space relationships among structural and metamorphic aureoles related to granite emplacement: a case study from the Serre Massif (southern Italy). *Geological Magazine*, *150*(03), 441–454. https://doi.org/10.1017/S0016756812000714

Festa, V., Cicala, M., & Tursi, F. (2020). The Curinga – Girifalco Line in the framework of the tectonic evolution of the remnant Alpine chain in Calabria (southern Italy). *International Journal of Earth Sciences*. https://doi.org/10.1007/s00531-020-01918-5

Festa, V., Messina, A., Paglionico, A., Piccarreta, G., & Rottura, A. (2004). Pre-Triassic history recorded in the Calabria-Peloritani segment of the Alpine chain, southern Italy. An overview. *Periodico Di Mineralogia*, *73*(SPEC. ISSUE 2), 57–71.

Festa, V., Tursi, F., Caggianelli, A., & Spiess, R. (2018). The tectono-magmatic setting of the Hercynian upper continental crust exposed in Calabria (Italy) as revealed by the 1:10,000 structural-geological map of the Levadio stream area. *Italian Journal of Geosciences*, *137*(2), 165–174. https://doi.org/10.3301/IJG.2018.03

Fornelli, A., Festa, V., Micheletti, F., Spiess, R., & Tursi, F. (2020). Building an orogen: Review of U-Pb zircon ages from the calabria-peloritani terrane to constrain the timing of the southern variscan belt. *Minerals*, *10*(11), 1–29. https://doi.org/10.3390/min10110944

Fornelli, A., Micheletti, F., & Piccarreta, G. (2007). The Neoproterozoic-Early Cambrian felsic magmatism in Calabria (Italy): Inferences as to the origin and geodynamic setting. *Periodico Di Mineralogia*, *76*(3), 99–112. https://doi.org/10.2451/2007PM0019

Giuntoli, F., Lanari, P., Burn, M., Barbara Eva, K., & Engi, M. (2018). Deeply subducted continental fragments - Part 2: Insight from petrochronology in the central Sesia Zone (western Italian Alps). *Solid Earth*, *9*(1), 191–222. https://doi.org/10.5194/se-9-191-2018

Graessner, T., & Schenk, V. (2001). *An Exposed Hercynian Deep Crustal Section in the Sila Massif of Northern Calabria: Mineral Chemistry, Petrology and a P-T Path of Granulite-facies Metapelitic Migmatites and Metabasites*. *Journal of Petrology* (Vol. 42). https://doi.org/10.1093/petrology/42.5.931

Green, E. C. R., White, R. W., Diener, J. F. A., Powell, R., Holland, T. J. B., & Palin, R. M. (2016). Activity-composition relations for the calculation of partial melting equilibria in metabasic rocks. *Journal of Metamorphic Geology*, *34*(9), 845–869. https://doi.org/10.1111/jmg.12211

Guiraud, M., Powell, R., & Rebay, G. (2001). H2O in metamorphism and unexpected behaviour in the preservation of metamorphic mineral assemblages. *Journal of Metamorphic Geology*, (19), 445–454. https://doi.org/10.1046/j.0263-4929.2001.00320.x

Harlov, D., Tropper, P., Seifert, W., Nijland, T., & Förster, H.-J. J. (2006). Formation of Al-rich titanite (CaTiSiO4O-CaAlSiO4OH) reaction rims on ilmenite in metamorphic rocks as a function of fH2O and fO2. *Lithos*, *88*(1–4), 72–84. https://doi.org/10.1016/j.lithos.2005.08.005

Holland, T. J. B., & Powell, R. (1998). An internally consistent thermodynamic data set for phases of petrological interest. *Journal of Metamorphic Geology*, *16*(3), 309–343. https://doi.org/10.1111/j.1525-1314.1998.00140.x

Holland, T. J. B., & Powell, R. (2003). Activity-compositions relations for phases in petrological calculations: An asymetric multicomponent formulation. *Contributions to Mineralogy and Petrology*, *145*(4), 492–501. https://doi.org/10.1007/s00410-003-0464-z

Holland, T. J. B., & Powell, R. (2011). An improved and extended internally consistent thermodynamic dataset for phases of petrological interest, involving a new equation of state for solids. *Journal of Metamorphic Geology*, *29*(3), 333–383. https://doi.org/10.1111/j.1525-1314.2010.00923.x

Holyoke, C. W., & Tullis, J. (2006). The interaction between reaction and deformation: An experimental study using a biotite + plagioclase + quartz gneiss. *Journal of Metamorphic Geology*, *24*(8), 743–762. https://doi.org/10.1111/j.1525-1314.2006.00666.x

Iannace, A., Reddy, S. M., Bonardi, G., Messina, A., Vitale, S., Somma, R., … D'Errico, M. (2007). The carbonate tectonic units of northern Calabria (Italy): a record of Apulian palaeomargin evolution and Miocene convergence, continental crust subduction, and exhumation of HP–LT rocks. *Journal of the Geological Society*, *164*(6), 1165–1186. https://doi.org/10.1144/0016-76492007-017

Langone, A., Caggianelli, A., Festa, V., & Prosser, G. (2014). Time Constraints on the Building of the Serre Batholith: Consequences for the Thermal Evolution of the Hercynian Continental Crust Exposed in Calabria (Southern Italy). *The Journal of Geology*, *122*(2), 183–199. https://doi.org/10.1086/675227

Langone, A., Gueguen, E., Prosser, G., Caggianelli, A., & Rottura, A. (2006). The Curinga-Girifalco fault zone (northern Serre, Calabria) and its significance within the Alpine tectonic evolution of the western Mediterranean. *Journal of Geodynamics*, *42*(4–5), 140–158. https://doi.org/10.1016/j.jog.2006.06.004

Le Goff, E., & Ballèvre, M. (1990). Geothermobarometry in albite-garnet orthogneisses: A case study from the Gran Paradiso nappe (Western Alps). *LITHOS*. https://doi.org/10.1016/0024-4937(90)90026-W

Leoni, L., Menichini, M., & Saitta, M. (2004). Ricalibrazione di una metodologia in fluorescenza-X per l'analisi di minerali e rocce su campioni di polvere. *Atti Della Società Toscana Di Scienze Naturali*, *109*, 13–20.

Leoni, L., & Saitta, M. (1976a). Determination of yttrium and niobium on standard silicate rocks by X-ray fluorescence analyses. *X-Ray Spectrometry*, *5*, 29–30.

Leoni, L., & Saitta, M. (1976b). X-ray fluorescence analysis of 29 trace elements in rock and mineral standards. *Rendiconti Della Societa Italiana Di Mineralogia e Petrologia*, *32*(2), 497–510.

Leydier, T., Goncalves, P., Lanari, P., & Oliot, E. (2019). On the petrology of brittle precursors of shear zones – An expression of concomitant brittle deformation and fluid–rock interactions in the 'ductile' continental crust? *Journal of Metamorphic Geology*, *37*(8), 1129–1149. https://doi.org/10.1111/jmg.12504

Liberi, F., Morten, L., & Piluso, E. (2006). Geodynamic significance of ophiolites within the Calabrian Arc. *Island Arc*, *15*(1), 26–43. https://doi.org/10.1111/j.1440-1738.2006.00520.x

Liberi, F., Piluso, E., & Langone, A. (2011). Permo-Triassic thermal events in the lower Variscan continental crust section of the Northern Calabrian Arc, Southern Italy: Insights from petrological data and in situ U-Pb zircon geochronology on gabbros. *Lithos*, *124*(3–4), 291–307. https://doi.org/10.1016/j.lithos.2011.02.016

Maldonado, R., Ortega-Gutiérrez, F., & Ortíz-Joya, G. A. (2018). Subduction of Proterozoic to Late Triassic continental basement in the Guatemala suture zone: A petrological and geochronological study of high-pressure metagranitoids from the Chuacús complex. *Lithos*, *308–309*, 83–103. https://doi.org/10.1016/j.lithos.2018.02.030

Massonne, H. J. (2015). Derivation of P-T paths from high-pressure metagranites - Examples from the Gran Paradiso Massif, western Alps. *Lithos*, *226*, 265–279. https://doi.org/10.1016/j.lithos.2014.12.024

Massonne, H. J., & Schreyer, W. (1987). Phengite geobarometry based on the limiting assemblage with K-feldspar, phlogopite, and quartz. *Contributions to Mineralogy and Petrology*, *96*(2), 212–224. https://doi.org/10.1007/BF00375235

Menold, C. A., Manning, C. E., Yin, A., Tropper, P., Chen, X. H., & Wang, X. F. (2009). Metamorphic evolution, mineral chemistry and thermobarometry of orthogneiss hosting ultrahigh-pressure eclogites in the North Qaidam metamorphic belt, Western China. *Journal of Asian Earth Sciences*, *35*(3–4), 273–284. https://doi.org/10.1016/j.jseaes.2008.12.008

Micheletti, F., Barbey, P., Fornelli, A., Piccarreta, G., & Deloule, E. (2007). Latest precambrian to early cambrian U-Pb zircon ages of augen gneisses from Calabria (Italy), with inference to the Alboran microplate in the evolution of the peri-Gondwana terranes. *International Journal of Earth Sciences*, *96*(5), 843–860. https://doi.org/10.1007/s00531-006-0136-0

Micheletti, F., Fornelli, A., Piccarreta, G., & Tiepolo, M. (2011). U-Pb zircon data of Variscan meta-igneous and igneous acidic rocks from an Alpine shear zone in Calabria (southern Italy). *International Journal of Earth Sciences*, *100*(1), 139–155. https://doi.org/10.1007/s00531-009-0497-2

Ortolano, G., Visalli, R., Fazio, E., Fiannacca, P., Godard, G., Pezzino, A., … Cirrincione, R. (2020). Tectono‐metamorphic evolution of the Calabria continental lower crust: the case of the Sila Piccola Massif. *International Journal of Earth Sciences*, 1–25.

https://doi.org/https://doi.org/10.1007/s00531-020-01873-1

Paglionico, A., & Piccarreta, G. (1976). Le Unità del Fiume Pomo e di Castagna nelle Serre settentrionali (Calabria). *Bollettino Della Societa Geologica Italiana*, *95*, 27–37.

Paglionico, A., & Piccarreta, G. (1978). History and petrology of a fragmant of the deep crust in the Serre (Calabria, southern Italy). *N. Jb. Miner. Mh.*, *9*, 385–396.

Palin, R. M., Weller, O. M., Waters, D. J., & Dyck, B. (2016). Quantifying geological uncertainty in metamorphic phase equilibria modelling; A Monte Carlo assessment and implications for tectonic interpretations. *Geoscience Frontiers*, *7*(4), 591–607. https://doi.org/10.1016/j.gsf.2015.08.005

Pattison, D. R. M., de Capitani, C., & Gaidies, F. (2011). Petrological consequences of variations in metamorphic reaction affinity. *Journal of Metamorphic Geology*, *29*(9), 953–977. https://doi.org/10.1111/j.1525-1314.2011.00950.x

Pattison, D. R. M., & Tinkham, D. K. (2009). Interplay between equilibrium and kinetics in prograde metamorphism of pelites: An example from the Nelson aureole, British Columbia. *Journal of Metamorphic Geology*, *27*(4), 249–279. https://doi.org/10.1111/j.1525-1314.2009.00816.x

Piccarreta, G. (1981). Deep-rooted overthrusting and blueschistic metamorphism in compressive continental margins. An example from Calabria (Southern Italy). *Geological Magazine*, *118*(5), 539–544. https://doi.org/10.1017/S0016756800032908

Pouchou, J.-L., & Pichoir, F. (1988). Microbeam analysis. In D. E. Newbury (Ed.), *A simplified version of the "PAP" model for matrix corrections in EPMA* (pp. 315–318). San Francisco: San Francisco Press.

Pouchou, J.-L., & Pichoir, F. (1991). Quantitative Analysis of Homogeneous or Stratified Microvolumes Applying the Model "PAP." In K. F. J. Heinrich & D. E. Newbury (Eds.), *Electron Probe Quantitation* (pp. 31–75). Boston, MA: Springer US. https://doi.org/10.1007/978-1-4899-2617-3_4

Powell, R., & Holland, T. J. B. (1988). A internally consistent thermodynamic dataset with uncertainties and correlation: 3 Application to geobarometry, worked examples and a computer program. *Journal of Metamorphic Geology*, *6*, 173–204.

Proyer, A. (2003). The preservation of high-pressure rocks during exhumation: Metagranites and metapelites. *Lithos*, *70*(3–4), 183–194.

https://doi.org/10.1016/S0024-4937(03)00098-7

Rubie, D. C. (1986). The catalysis of mineral reactions by water and restrictions on the presence of aqueous fluid during metamorphism. *Mineralogical Magazine*, *50*(357), 399–415. https://doi.org/10.1180/minmag.1986.050.357.05

Schenk, V. (1980). U-Pb and Rb-Sr radiometric dates and their correlation with metamorphic events in the granulite-facies basement of the serre, Southern Calabria (Italy). *Contributions to Mineralogy and Petrology*, *73*(1), 23–38. https://doi.org/10.1007/BF00376258

Schenk, V. (1981). Synchronous uplift of the lower crust of the Ivrea Zone and of Southern Calabria and its possible consequences for the Hercynian orogeny in Southern Europe. *Earth and Planetary Science Letters*, *56*(C), 305–320. https://doi.org/10.1016/0012-821X(81)90136-9

Schenk, V. (1990). The exposed crustal cross section of southern Calabria, Italy: structure and evolution of a segment of Hercynian crust. In M. H. Sallisbury & D. M. Fountain (Eds.), *Exposed Cross-Sections of the Continental Crust* (pp. 21–42). Kluwer Academic Publishers. https://doi.org/10.1007/978-94-009-0675-4

Spiegel, C. (2003). Mylonitization, dry shearing and the exhumation of the former lower crust: The Curinga-Girifalco Line (Calabria, South Italy). *Neues Jahrbuch Fur Geologie Und Palaontologie - Abhandlungen*, *230*(2–3), 359–390. https://doi.org/10.1127/njgpa/230/2003/359

Thomson, S. N. (1998). Assessing the nature of tectonic contacts using fission-track thermochronology: An example from the Calabrian Arc, southern Italy. *Terra Nova*, *10*(1), 32–36. https://doi.org/10.1046/j.1365-3121.1998.00165.x

Tursi, F., Bianco, C., Brogi, A., Caggianelli, A., Prosser, G., Ruggieri, G., & Braschi, E. (2020). Cold subduction zone in northern Calabria (Italy) revealed by lawsonite–clinopyroxene blueschists. *Journal of Metamorphic Geology*, *38*(5), 451–469. https://doi.org/10.1111/jmg.12528

Tursi, F., Festa, V., Fornelli, A., Micheletti, F., & Spiess, R. (2018). Syn-shearing mobility of major elements in ductile shear zones : state of the art for felsic deformed protoliths. *Periodico Di Mineralogia*, *87*(November), 289–308. https://doi.org/10.2451/2018PM811

Tursi, F., Spiess, R., Festa, V., & Fregola, R. A. (2020). Hercynian subduction-related processes within the metamorphic continental crust in Calabria (southern Italy). *Journal of Metamorphic Geology*, *38*(7), 771–793. https://doi.org/10.1111/jmg.12537

Wakabayashi, J. (2004). Tectonic mechanisms associated with P-T paths of regional metamorphism: Alternatives to single-cycle thrusting and heating. *Tectonophysics*, *392*, 193–218. https://doi.org/10.1016/j.tecto.2004.04.012

Waters, D. J., & Lovegrove, D. P. (2002). Assessing the extent of disequilibrium and overstepping of prograde metamorphic reactions in metapelites from the Bushveld Complex aureole , South Africa. *Journal of Metamorphic Geology*, *20*(1), 135–149.

White, R. W., Powell, R., & Johnson, T. E. (2014). The effect of Mn on mineral stability in metapelites revisited: New a-x relations for manganese-bearing minerals. *Journal of Metamorphic Geology*, *32*(8), 809–828. https://doi.org/10.1111/jmg.12095

Willner, A. P., Glodny, J., Gerya, T. V., Godoy, E., & Massonne, H. J. (2004). A counterclockwise PTt path of high-pressure/low-temperature rocks from the Coastal Cordillera accretionary complex of south-central Chile: Constraints for the earliest stage of subduction mass flow. *Lithos*, *75*(3–4), 283–310. https://doi.org/10.1016/j.lithos.2004.03.002

Xia, Q. X., Zheng, Y. F., Lu, X. N., Hu, Z., & Xu, H. (2012). Formation of metamorphic and metamorphosed garnets in the low-T/UHP metagranite during continental collision in the Dabie orogen. *Lithos*, *136–139*, 73–92. https://doi.org/10.1016/j.lithos.2011.10.004

Young, D. J., & Kylander-Clark, A. R. C. (2015). Does continental crust transform during eclogite facies metamorphism? *Journal of Metamorphic Geology*, *33*(4), 331–357. https://doi.org/10.1111/jmg.12123

Zucali, M. (2011). Coronitic microstructures in patchy eclogitised continental crust: The Lago della Vecchia pre-Alpine metagranite (Sesia-Lanzo Zone, Western Italian Alps). *Journal of the Virtual Explorer*, *38*. https://doi.org/10.3809/jvirtex.2011.00286

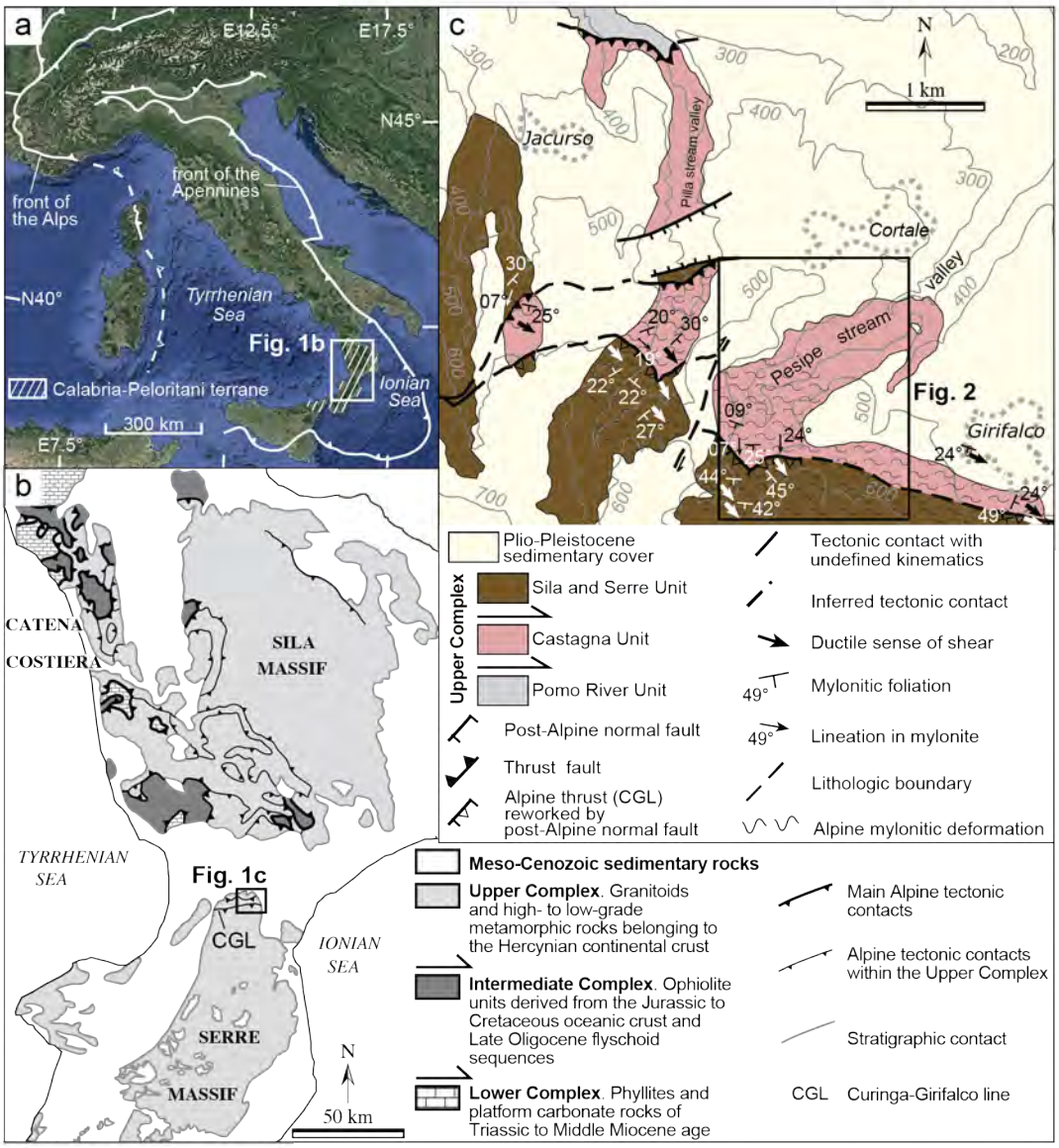

jmg_12596_f1.png

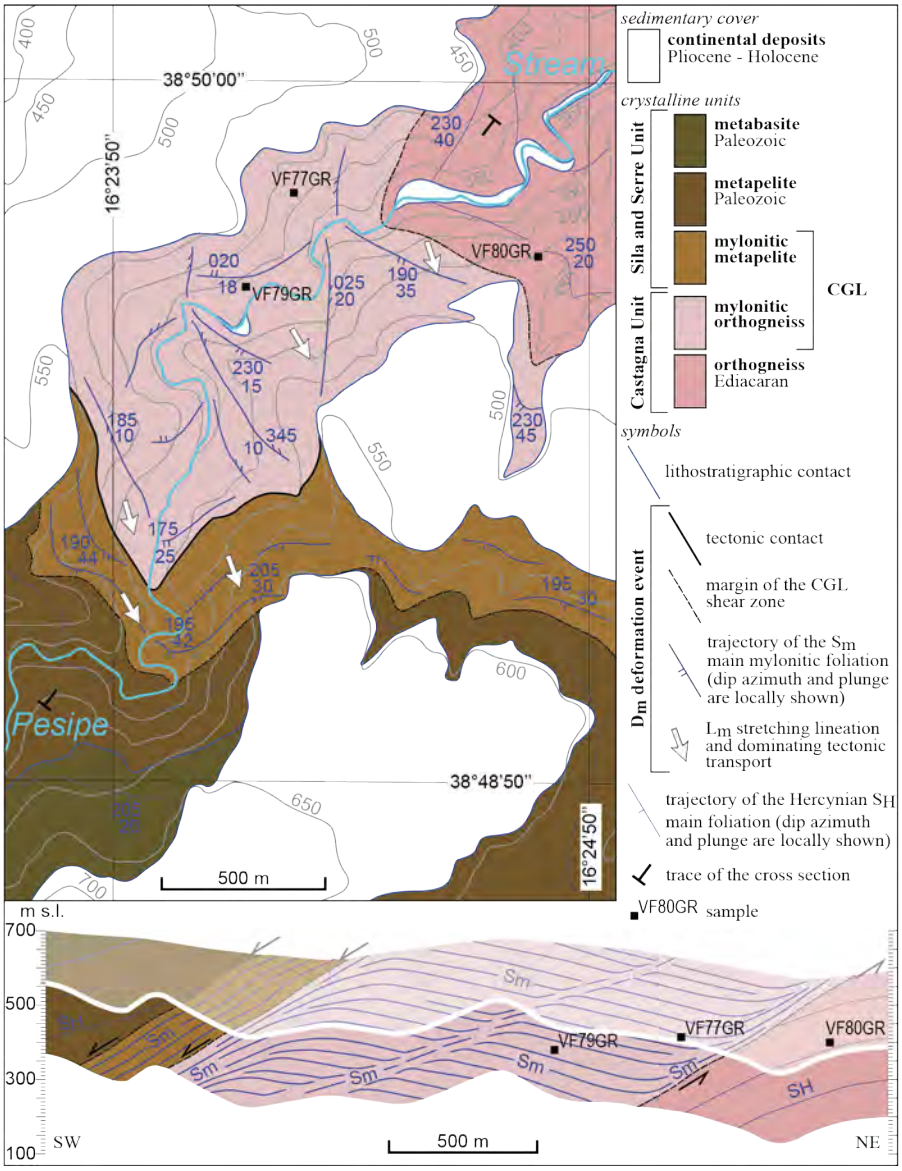

jmg_12596_f2.png

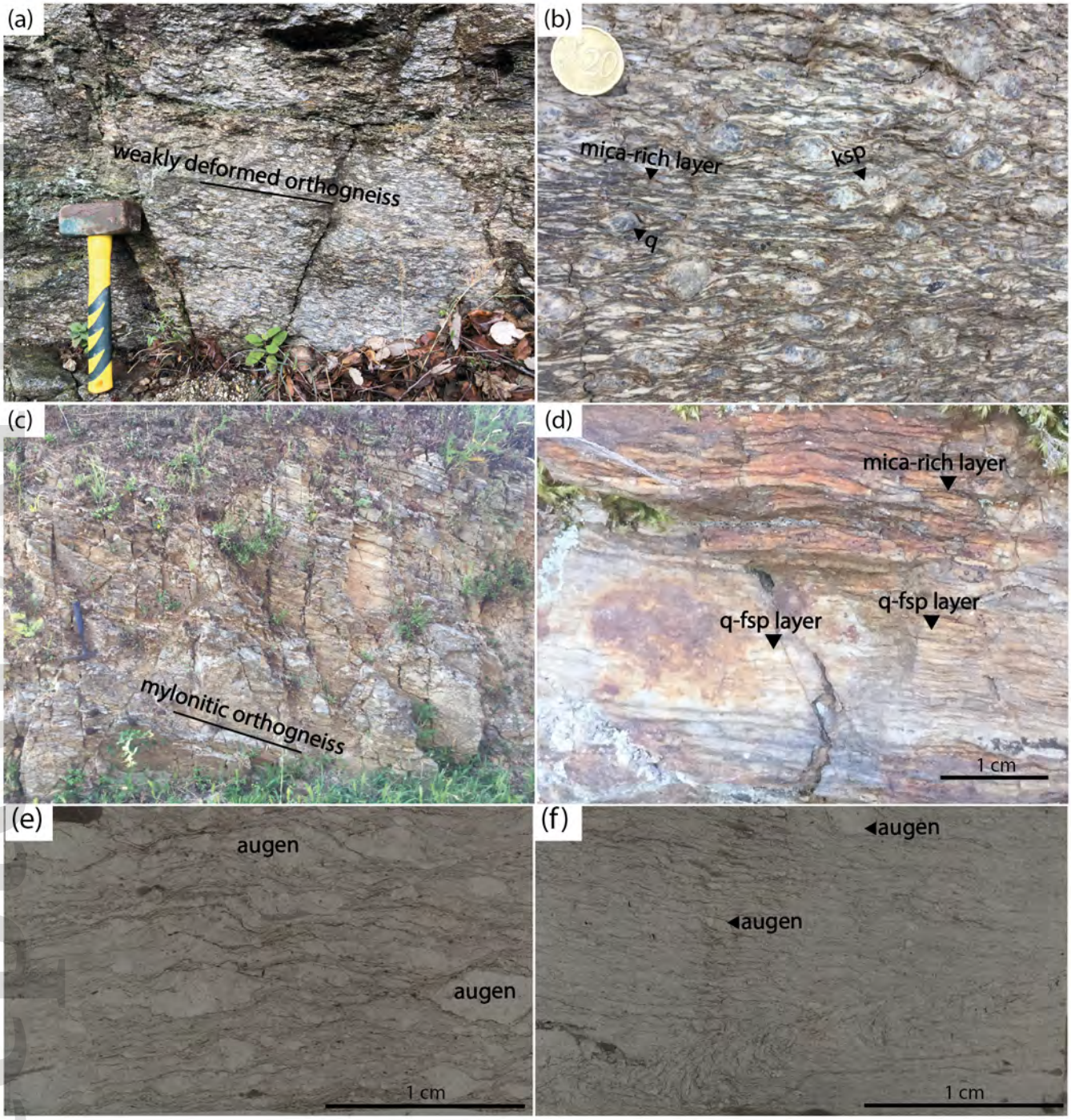

jmg_12596_f3.png

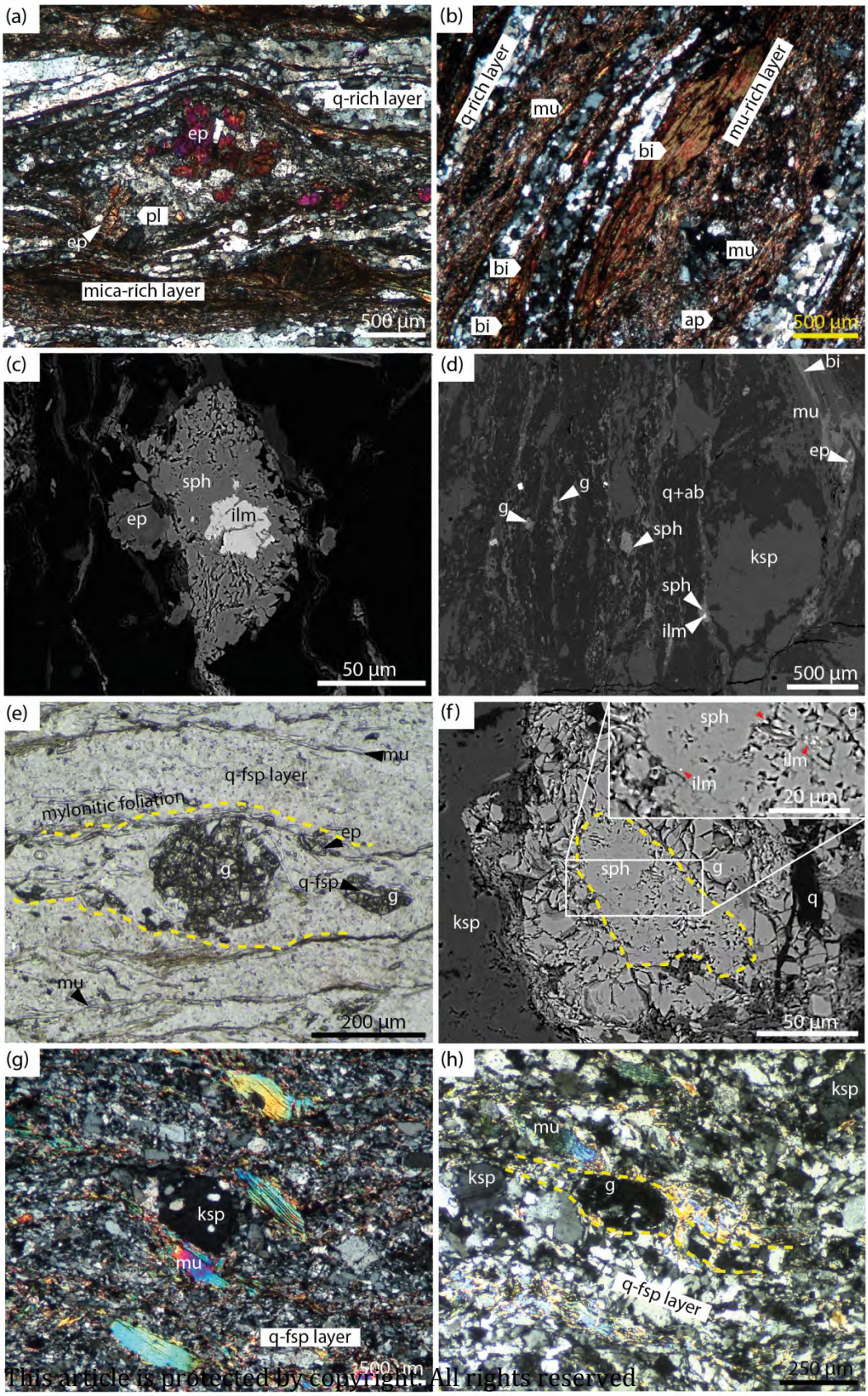

jmg_12596_f4.png

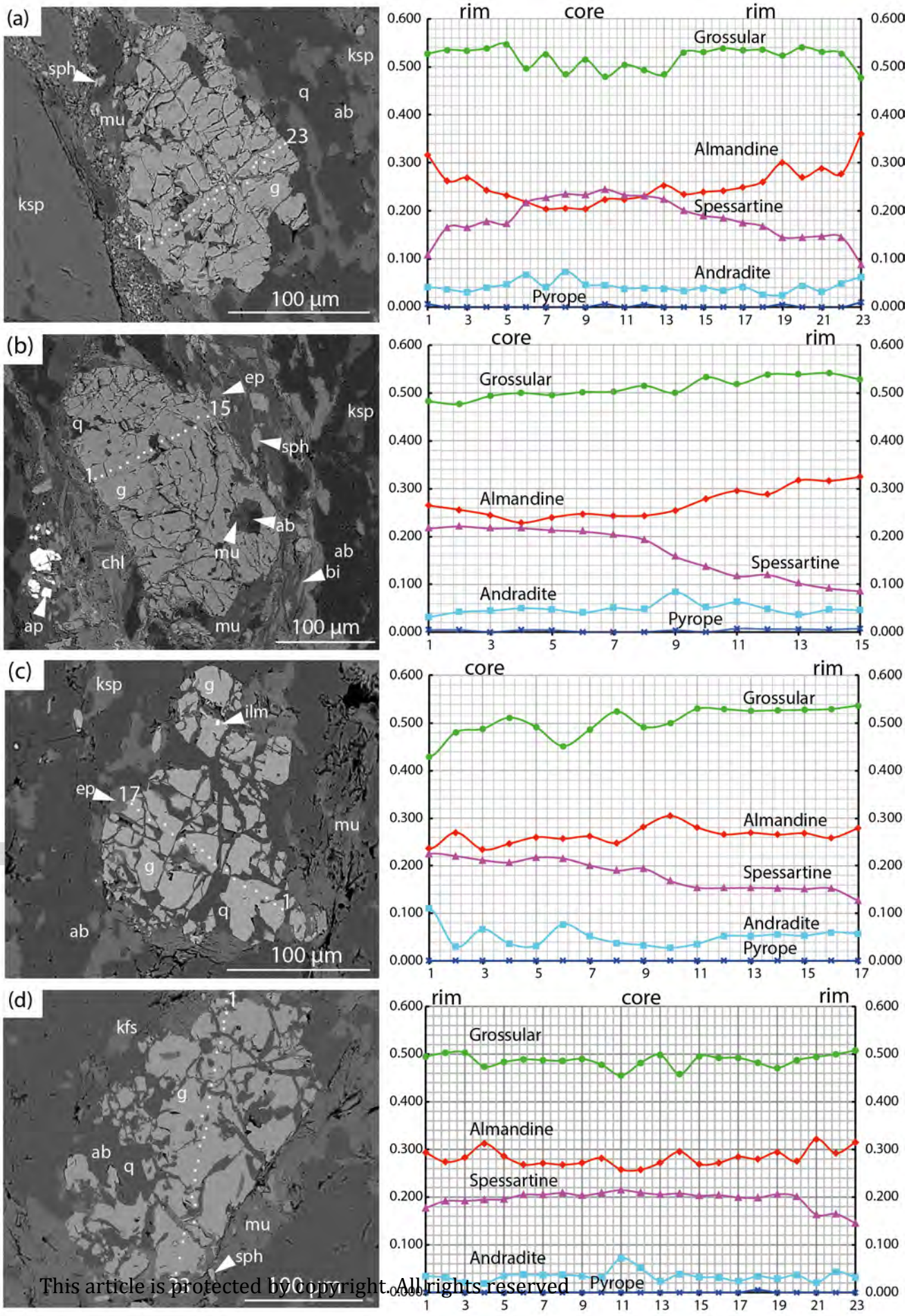

jmg_12596_f5.png

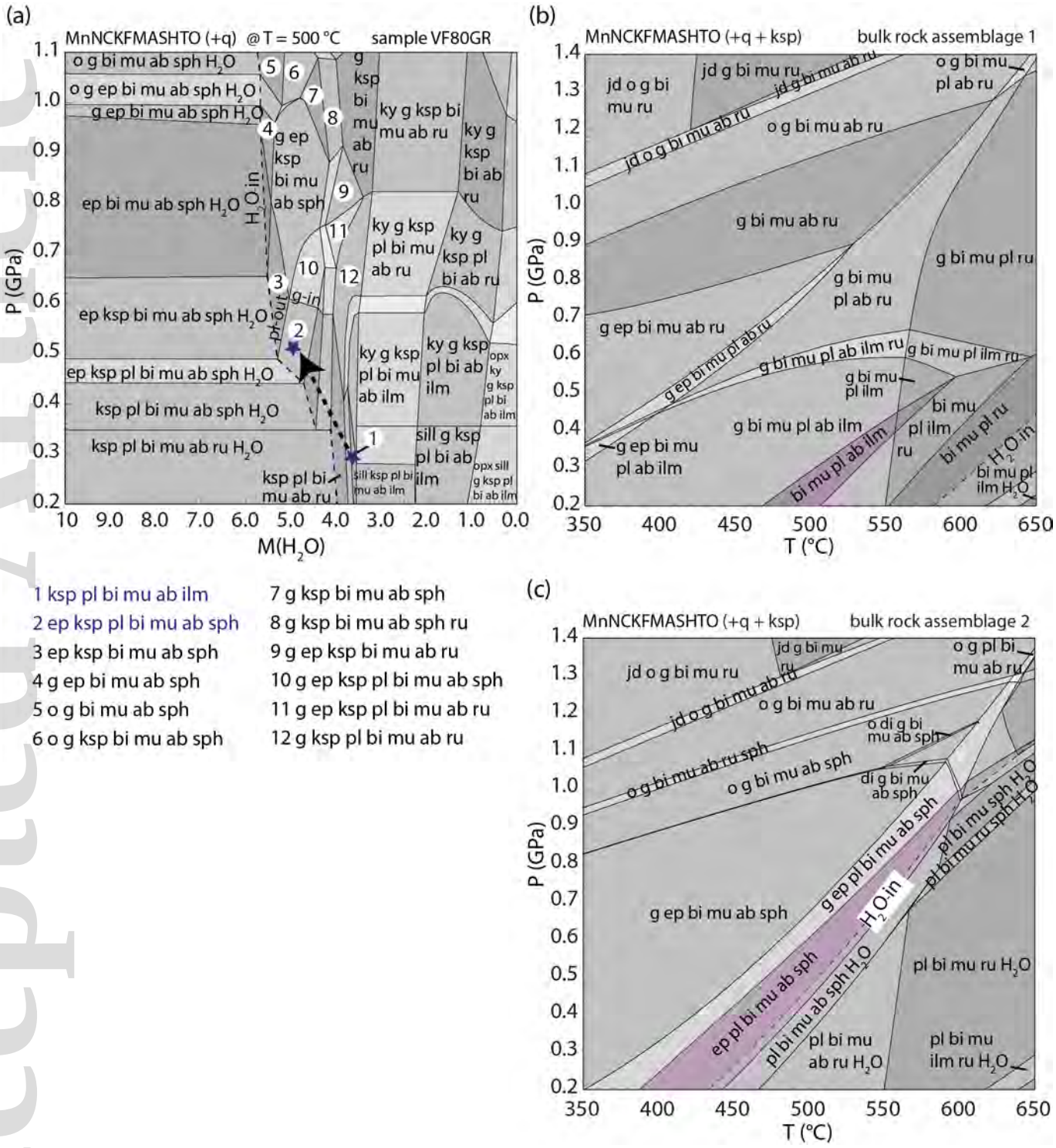

1 ksp pl bi mu ab ilm
2 ep ksp pl bi mu ab sph
3 ep ksp bi mu ab sph
4 g ep bi mu ab sph
5 o g bi mu ab sph
6 o g ksp bi mu ab sph
7 g ksp bi mu ab sph
8 g ksp bi mu ab sph ru
9 g ep ksp bi mu ab ru
10 g ep ksp pl bi mu ab sph
11 g ep ksp pl bi mu ab ru
12 g ksp pl bi mu ab ru

jmg_12596_f6.png

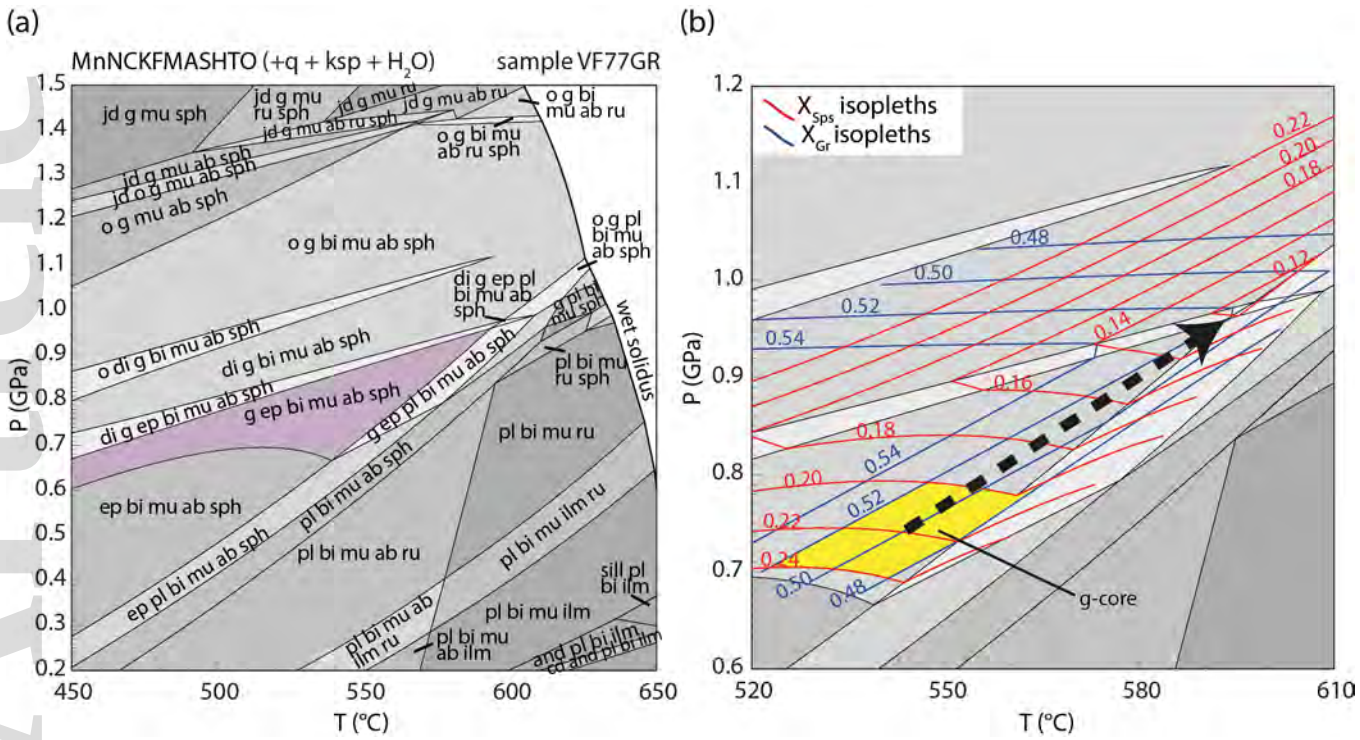

jmg_12596_f7.png

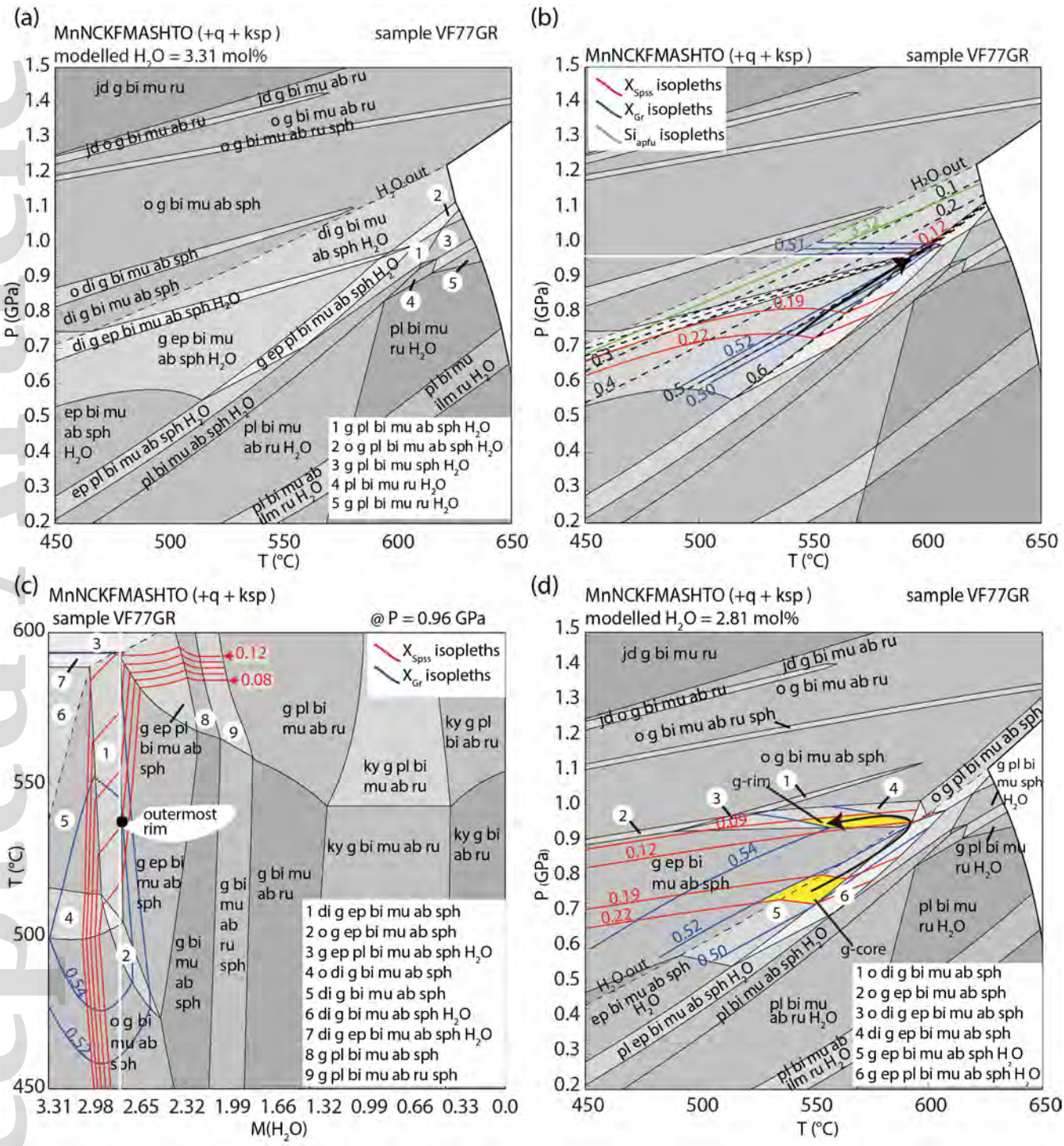

jmg_12596_f8.png

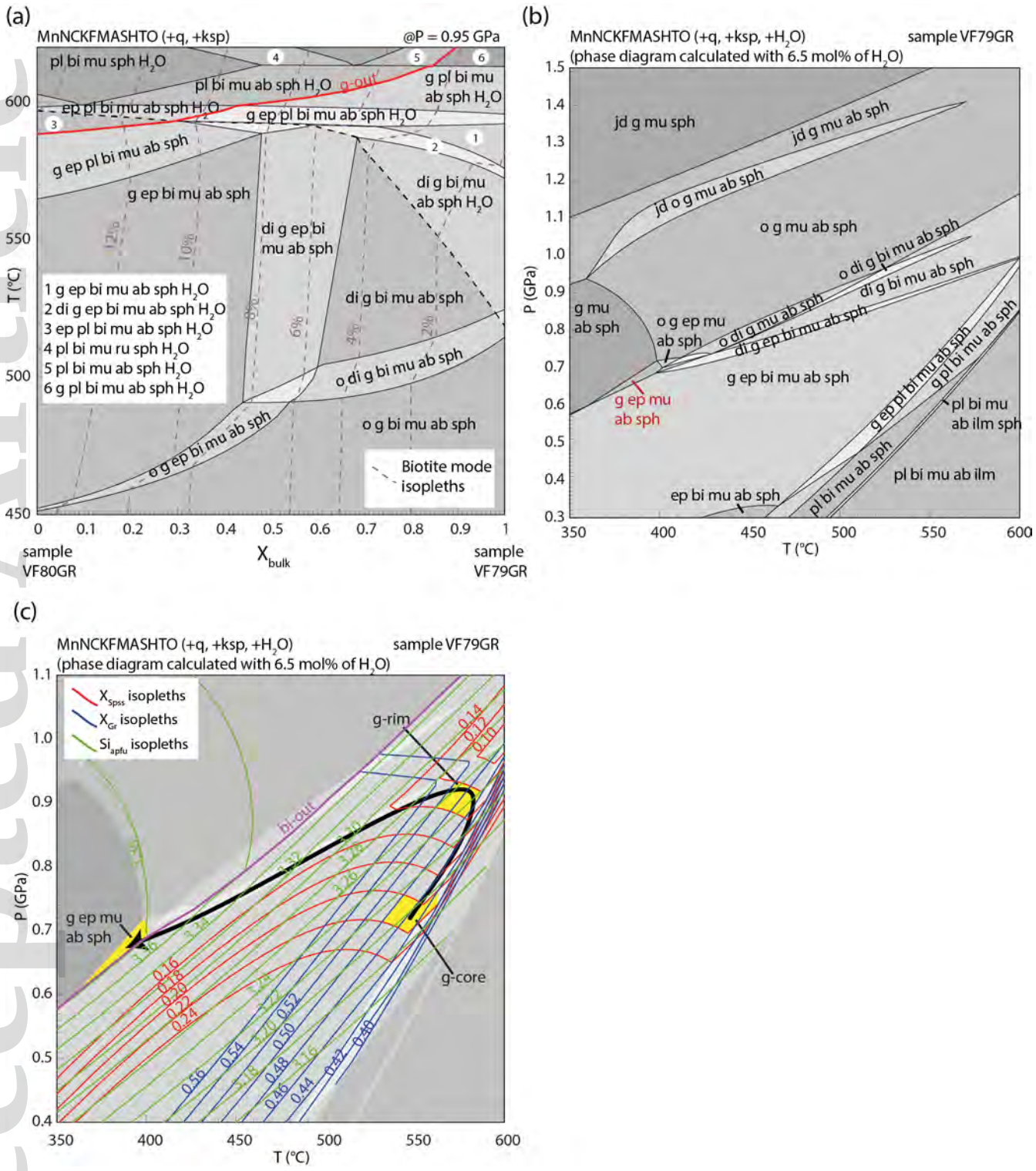

jmg_12596_f9.png

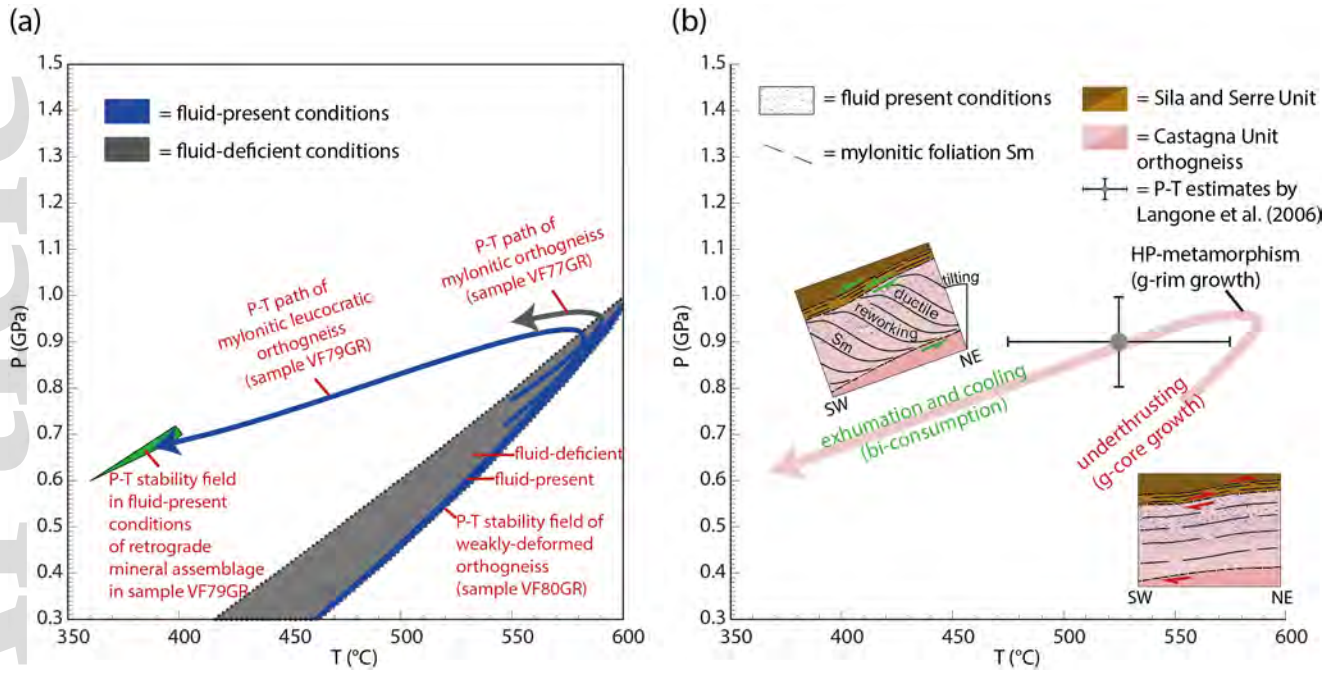

jmg_12596_f10.png